Exosomes derived from magnetically actuated bone mesenchymal stem cells promote tendon-bone healing through the miR-21-5p/SMAD7 pathway

Xiang-Dong Wu [a], Lin Kang [b], Jingjing Tian [b], Yuanhao Wu [b], Yue Huang [a], Jieying Liu [b], Hai Wang [a,*], Guixing Qiu [a,**], Zhihong Wu [b,c,***]

[a] Department of Orthopaedic Surgery, Peking Union Medical College Hospital, Chinese Academy of Medical Sciences & Peking Union Medical College, Beijing, 100730, China
[b] Medical Science Research Center (MRC), Peking Union Medical College Hospital, Chinese Academy of Medical Sciences & Peking Union Medical College, Beijing, 100730, China
[c] Beijing Key Laboratory for Genetic Research of Skeletal Deformity, Beijing, 100730, China

ARTICLE INFO

ABSTRACT

Graft healing after anterior cruciate ligament reconstruction (ACLR) involves slow biological processes, and various types of biological modulations have been explored to promote tendon-to-bone integration. Exosomes have been extensively studied as a promising new cell-free strategy for tissue regeneration, but few studies have reported their potential in tendon-to-bone healing. In this study, a novel type of exosome derived from magnetically actuated (iron oxide nanoparticles (IONPs) combined with a magnetic field) bone mesenchymal stem cells (BMSCs) (IONP-Exos) was developed, and the primary purpose of this study was to determine whether IONP-Exos exert more significant effects on tendon-to-bone healing than normal BMSC-derived exosomes (BMSC-Exos). Here, we isolated and characterized the two types of exosomes, conducted in vitro experiments to measure their effects on fibroblasts (NIH3T3), and performed in vivo experiments to compare the effects on tendon-to-bone integration. Moreover, functional exploration of exosomal miRNAs was further performed by utilizing a series of gain- and loss-of-function experiments. Experimental results showed that both BMSC-Exos and IONP-Exos could be shuttled intercellularly into NIH3T3 fibroblasts and enhanced fibroblast activity, including proliferation, migration, and fibrogenesis. In vivo, we found that IONP-Exos significantly prevented peri-tunnel bone loss, promoted more osseous ingrowth into the tendon graft, increased fibrocartilage formation at the tendon-bone tunnel interface, and induced a higher maximum load to failure than BMSC-Exos. Furthermore, overexpression of miR-21-5p remarkably enhanced fibrogenesis in vitro, and SMAD7 was shown to be involved in the promotive effect of IONP-Exos on tendon-to-bone healing. Our findings may provide new insights into the regulatory roles of IONPs in IONP-Exos communication via stimulating exosomal miR-21-5p secretion and the SMAD7 signaling pathway in the fibrogenic process of tendon-to-bone integration. This work could provide a new strategy to promote tendon-to-bone healing for tissue engineering in the future.

1. Introduction

The 24th Winter Olympics officially ended with the traditional closing ceremony. As an international event full of extreme sports, involving high-speed collisions, spectacular spills, and frightening falls, the Winter Olympics has seen its fair share of major sports injuries [1,2]. Among them, anterior cruciate ligament (ACL) injury is one of the most common injuries of the knee joint, which not only causes knee pain and joint instability, but also increases the risk of knee osteoarthritis and disability [3,4]. Anterior cruciate ligament reconstruction (ACLR) is considered a

* Corresponding author. Department of Orthopaedic Surgery, Peking Union Medical College Hospital, Chinese Academy of Medical Sciences & Peking Union Medical College; No.1 Shuaifuyuan, Beijing 100730, China.
** Corresponding author. Department of Orthopaedic Surgery, Peking Union Medical College Hospital, Chinese Academy of Medical Sciences & Peking Union Medical College; No.1 Shuaifuyuan, Beijing 100730, China.
*** Corresponding author. Medical Science Research Center (MRC), Peking Union Medical College Hospital, Chinese Academy of Medical Sciences & Peking Union Medical College; No.1 Shuaifuyuan, Beijing 100730, China.
E-mail addresses: wanghai907@hotmail.com (H. Wang), qguixing@126.com (G. Qiu), wuzh3000@126.com (Z. Wu).

safe and effective surgical procedure for the management of ACL injury, and tendon autografts are widely used and considered the current "gold standard" in ACLR [5–7]. Over 120,000 ACL injuries occur each year in the US, with more than 2.6 million worldwide, and approximately 800, 000 ACLR surgeries are performed per year globally [8,9]. However, the lack of graft incorporation remains a cause of failure after ACLR, especially in the initial phase of rehabilitation [10–12].

Tendon graft-to-bone tunnel integration after ACLR involves slow biological processes consisting of three key healing processes and requires more than 12 months for graft maturation [13–17]. Therefore, there has been substantial interest in exploring biological strategies, including drugs, growth factors, platelet-rich plasma (PRP), stem cells, stem cell-conditioned media, biomaterials, and biophysical interventions, to facilitate tendon graft-to-bone tunnel integration and promote earlier graft maturation, which may allow earlier recovery and earlier return to play [18–26]. Among these agents, mesenchymal stem cells (MSCs) have attracted much research interest and have been widely used in the field of tissue engineering mainly because they have the capacity to proliferate, self-renew, and differentiate into various tissues. Previous studies have investigated several different types of stem cells for the promotion of graft healing after ACLR in different animal models and reported significant enhancement of tendon-to-bone integration shown by histology, biomechanics, imaging, and biochemistry during the early phase [27–29]. However, despite the great promise for tissue engineering and regenerative medicine, stem cell therapy remains not a therapeutic option mainly due to potential lethal adverse events, including tumor formation, unwanted immune responses, thrombotic complications, and transmission of adventitious agents, which have not yet been solved [30–32].

Given that there remain potential unresolved risks related to MSCs applications and that the regenerative effects of MSCs largely depend on paracrine factors, including growth factors, cytokines, and extracellular vesicles (EVs), recent regenerative medicine-related research is increasingly focusing on exosomes [33]. Exosomes are small (30–150 nm) membranous EVs that have been found to serve as carriers of macromolecules, including proteins, mRNAs, microRNAs (miRNAs), lipids, signaling cytokines, and serve as essential messengers between cells [34, 35]. As researchers found that exosomes released by stem cells rather than stem cells, play an essential role in stimulating regenerative responses, exosome therapy became an alternative for regenerative medicine [36]. More recently, several previous studies have investigated the effects of MSCs-derived exosomes on tendon injuries, and demonstrated that exosomes promote high-quality healing of injured tendons [37–39]. However, tendon-to-bone integration is more challenging as it takes place between inhomogeneous tissues, which is much slower than the tendon-to-tendon or bone-to-bone healing process that occurs within homogenous tissue [40]. Therefore, special attention has been given to augmenting tendon-to-bone insertion healing. A previous study utilized a low-frequency static magnetic field as a contact-free technology and mechanical stimulation to modulate cell physiology and found that magnetic therapy fine-tuned the tendon cell behavior through modulation of the inflammatory response [23]. Additional studies further induced a magnetically actuated system by combining a pulsed electromagnetic field and magnetic responsive membranes to modulate the inflammatory profile of tendon cells and macrophages, and suggested that the magnetically actuated system regulated inflammatory events and stimulated tendon regeneration [41,42]. In addition, a previous study found that incorporating iron oxide nanoparticles (IONPs) and a static magnetic field (SMF) significantly promoted wound healing by improving fibrogenesis and angiogenesis [43]. A comprehensive review highlighted the potential applications of magnetic nanoparticles and scaffolds with magnetic fields and stem cells for improved bone repair and regeneration [44]. Similarly, our previous study showed that SMF enhanced osteogenic differentiation through the upregulation of SMAD4 expression, and that exosomes derived from bone mesenchymal stem cells (BMSCs) stimulated with Fe_3O_4 nanoparticles and SMF significantly promoted wound healing, enhanced osteogenesis and angiogenesis compared to normal exosomes derived from BMSCs [45–47]. On these grounds, we hypothesized that compared with normal exosomes derived from BMSCs (BMSC-Exos), exosomes derived from magnetically actuated BMSCs (IONPs-incorporated BMSCs under a magnetic field (IONP-Exos)) might exhibit superior performance in tendon graft-to-bone regeneration and integration, which might ultimately lead to enhanced tendon graft-bone healing.

2. Materials and methods

2.1. Cell culture

Human BMSCs were purchased from ScienCell Research Laboratories (ScienCell, Carlsbad, CA, USA) and cultured according to the manufacturer's instructions. Briefly, BMSCs were cultured in MSCs medium (ScienCell) containing 5% fetal bovine serum (FBS), 1% mesenchymal stem cell growth supplement, and 1% penicillin/streptomycin. BMSCs in passages three to six were used for the in vitro experiments. The NIH3T3 fibroblast cell line was obtained from the Cell Bank of Type Culture Collection of the Chinese Academy of Sciences (Beijing, China) and cultured in Dulbecco's modified Eagle's medium (DMEM, Gibco, Invitrogen, Carlsbad, CA, USA) with 10% FBS (Gibco) and 1% penicillin-streptomycin (Gibco). All cells were cultured at 37 °C with 5% CO_2 concentration, and passaged every 2–3 days when they reached approximately 90% confluence.

2.2. Internalization of IONPs in BMSCs under SMF

IONPs (magnetite Fe_3O_4) were synthesized by Ruixi Biological Technology (Xi'an Ruixi Biological Technology, Xi'an, China). According to the manufacturer, anionic polyelectrolyte poly (4-styrenesulfonic acid-co-maleic acid) sodium salt (PSSMA) was used for surface modification of IONPs, which not only prevents oxidation and agglomeration of IONPs, but also improves their functionalization, making them well dispersed in water, phosphate buffered saline (PBS), and ethanol. As previously described, the SMF environment was achieved by assembling a permanent neodymium magnet under the cell culture plates, and the desired effective SMF intensity was reached by adjusting the distance between the magnet and plate, and the intensity of the SMF was measured by using a Tesla meter (HT20; Hengtong, Suzhou, China) [46]. The nanoparticle zeta potential was measured using a Nano-ZS instrument (Malvern Instruments, Ltd., Malvern, UK), and the particle size was measured using a ZetaView Analyzer (Particle Metrix, Meerbusch, Germany). The morphology of BMSCs after engulfing IONPs was observed after co-treatment with IONPs and SMF. For detection of the internalized IONPs, the BMSCs-IONPs were visualized using transmission electron microscopy (TEM, Hitachi, Tokyo, Japan). Additionally, BMSCs were extensively washed with PBS three times to remove any free IONPs, and the cells were fixed in 10% formaldehyde for 30 min at room temperature and washed with deionized water three times. Then, Prussian blue staining was performed to further observe the internalized IONPs in the BMSCs.

2.3. Cell viability assay

Cell proliferation assay was performed to explore the cytotoxicity of the IONPs in BMSCs with Cell Counting Kit-8 (CCK-8; Dojindo, Tokyo, Japan). Briefly, BMSCs were seeded in 96-well plates (5000 cells/well), and IONPs were added to the culture medium at concentrations of 0, 10, 20, 30, 40, 50, 80, 100, and 120 μg/mL. After culturing for different durations, the culture medium was removed, and the cells were washed with PBS three times to remove free IONPs that did not enter the cells. Then, the viability of the IONPs-incorporated BMSCs was determined by a CCK-8 assay after the treatment mentioned above. Fresh culture medium with 10% CCK-8 assay reagent was added and incubated for 1 h,

and then the incubated medium was transferred to a new 96-well plate to avoid any disturbance of the cells. The absorbance was measured at 450 nm using a microplate reader (Bio-Rad Laboratories, Inc., Hercules, CA, USA). Based on the results of the CCK-8 assay, a concentration of 10–30 μg/mL was potentially beneficial for proliferation. Then, different strengths of SMF stimulation (0, 50, 100, and 200 mT) were used in combination with varying concentrations of IONPs (0, 10, 20, and 30 μg/mL) to further culture BMSCs to determine the optimal culture conditions, and cell proliferation was measured again as described above. Subsequently, the optimal concentrations of IONPs in combination with the optimal strength of SMF constitute the optimal magnetically actuated system and culture condition.

2.4. Exosome isolation and purification

The isolation and purification of exosomes were performed as previously described [45,47]. Briefly, after passage, BMSCs were cultured under standard conditions within 24 h. When the confluence of BMSCs reached 70–80%, the complete medium was discarded, the cells were washed and replaced with complete fresh medium supplemented with 10% exosome-depleted FBS (SBI System Biosciences, USA), and the cells were cultured for an additional 48 h at 37 °C and 5% CO$_2$. Then, the above-conditioned medium was collected for exosome isolation through four consequent centrifugation steps: (1) centrifugation at 300 g for 10 min at 4 °C to pellet dead cells and bulky debris; (2) centrifugation at 2000 g for 10 min at 4 °C to eliminate cell debris and large vesicles; (3) centrifugation at 10,000 g for 30 min to remove microvesicles, with the supernatant collected and filtered through 0.22-μm filters (Merck, Millipore Corporation, Bedford, MA, USA) to remove contaminating apoptotic bodies, microvesicles, and cell debris; (4) ultracentrifugation at 110,000 g for 70 min (Optima XPN, Beckman, Brea, CA, USA) at 4 °C, with the resulting pellet was resuspended in a large amount of PBS. A repeated 110,000 g ultracentrifugation was applied to purify the exosome preparation from the lower mobility fractions, mainly from free proteins. Exosome pellets were resuspended in PBS and stored at −80 °C.

2.5. Exosomes characterization and internalization

Morphology of the isolated exosomes was investigated by TEM. The absolute size distribution of the exosomes was measured by nanoparticle tracking analysis (NTA) using a ZetaView (Particle Metrix) and analyzed using the corresponding software ZetaView. Western blot analysis was then used to identify exosomal surface markers with the following primary antibodies CD9, CD81, Hsp70, and TSG101 (Exosome Panel, Abcam, Cambridge, UK).

To track the endocytosis of exosomes and quantify the efficiency of exosomes internalization by NIH3T3 fibroblasts, exosomes were labeled with fluorescent dye using the PKH26 Red Fluorescent Cell Linker Kit (Sigma, St Louis, MO, USA) according to the manufacturer's instructions. After labeling, the exosomes were washed with PBS and then ultracentrifuged at 110,000 g at 4 °C for 70 min to remove the unbound dye. Then, the PKH26-labeled exosomes were incubated with NIH3T3 fibroblasts for 4, 8, 12, 16, and 24 h, respectively. The cells were stained with FITC phalloidin (Sigma) and counterstained with 4,6-diamidino-2-phenylindole (DAPI, Sigma); the uptake of exosomes was observed using a confocal fluorescence microscope (Nikon, Tokyo, Japan).

2.6. Cell proliferation assay

Cell proliferation assay was used to evaluate the effect of IONP-Exos and BMSC-Exos on NIH3T3 fibroblast proliferation. NIH3T3 fibroblasts were seeded at 3000 cells/well into 96-well plates and allowed to proliferate for 24 h. Then, IONP-Exos (100 μg/mL), BMSC-Exos (100 μg/mL), or PBS were added to the wells and cultured for an additional 1, 3,

or 5 days. CCK-8 (Dojindo) was used for cell proliferation assays, and cell proliferation was calculated from the absorbance at 450 nm using a microplate reader.

2.7. Transwell assay

Transwell migration assay was used to measure the effect of IONP-Exos and BMSC-Exos on NIH3T3 fibroblast migration and was performed according to the manufacturer's recommendation. Briefly, a total of 5 × 10^4 NIH3T3 fibroblasts were seeded in the upper chamber of the transwell (Corning, NY, USA) with 100 μL of serum-free medium. In the lower chamber, 600 μL of culture medium containing 10% exosome-depleted FBS (SBI, USA) and IONP-Exos (100 μg/mL), BMSC-Exos (100 μg/mL), or the equivalent volume of exosome diluent (PBS) were added and incubated for 24 h. Fibroblasts on the permeable membrane of the upper chamber were gently wiped off using a cotton swab, and fibroblasts that migrated to the bottom of the filter membrane were fixed with anhydrous ethanol and stained with crystal violet (Beyotime, Shanghai, China). Five fields of the underside of the membrane were randomly selected, and the migrated cells were counted under a microscope.

2.8. Scratch wound healing assay

The scratch wound assay was used to evaluate the effect of IONP-Exos on NIH3T3 fibroblast migration. Briefly, fibroblasts were seeded at 3 × 10^5 cells/well into six-well plates, and when the cells had reached approximately 90% confluence, a sterile 200 μL pipette tip was used to scratch the cells across each well vertically. After washing each well twice with PBS to remove non-adherent cells, fresh serum-free medium containing IONP-Exos (100 μg/mL), BMSC-Exos (100 μg/mL), or PBS was added, respectively. The cell migration images were recorded at 0, 12, and 24 h after the scratch, and ImageJ software (NIH, Bethesda, MD, USA) was utilized to measure the wound area compared with the initial wound area.

2.9. qRT-PCR analysis

Total RNA from cells or exosomes was extracted using TRIzol reagent (Invitrogen). For the mRNA analysis, total RNA was reverse-transcribed into complementary cDNA using a PrimeScript RT reagent Kit (TaKaRa, Tokyo, Japan) according to the manufacturer's instructions. For the miRNA analysis, the isolated miRNA was reversely transcribed using the Mir-X miRNA First-Strand Synthesis Kit (Clontech, Mountain View, CA, USA). All RT-qPCR analyses were performed on an ABI system using SYBR Green Real-time PCR Master Mix (TaKaRa) according to the manufacturer's instructions. The relative expression level of mRNA or miRNA was normalized to an internal reference GAPDH or U6, and calculated using the $2^{-\Delta\Delta CT}$ method. The primer sequences used in this study are listed in the supplementary materials (Supplementary Tables 1 and 2).

2.10. Western blot analysis

The cultured cells were harvested, and proteins were isolated using RIPA lysis solution (Sigma). Protein concentrations were determined using a BCA Protein Assay Reagent Kit (Beyotime). Equal amounts of protein were separated by precast 4–12% Bis-Tris gels (NuPage, Invitrogen) and transferred to NuPage 0.45 μm nitrocellulose membranes (Invitrogen). The membranes were blocked with 5% non-fat milk in Tris-buffered saline containing 0.1% Tween 20 (TBST) for 1 h and incubated with primary antibodies overnight at 4 °C, and finally incubated with HRP-linked secondary antibodies for 1 h at room temperature. After incubation, the protein bands were visualized using an enhanced

chemiluminescence detection system (SuperSignal West Pico, Thermo Scientific). All protein expression was normalized to the internal control, GAPDH.

2.11. Animal experiments

The animal experiments were approved by the Animal Experimentation Ethics Committee of the Peking Union Medical College Hospital (No. XHDW-2021-061). All experiments were conducted in accordance with the principles and procedures outlined in the Guide for the Care and Use of Laboratory Animals of the National Institute of Health. This study followed the ARRIVE guidelines for reporting pre-clinical animal research [48]. Sprague-Dawley rats (male, 12 weeks old) underwent unilateral ACL resection followed by isometric ACLR using an ipsilateral flexor digitorum longus tendon autograft, which was conducted as previously described [48–50]. First, a longitudinal skin incision was made on the medial aspect of the distal leg, and the flexor digitorum longus tendon was identified and cut just distal to the ankle. The total length of the flexor digitorum longus tendon was then harvested as a graft (average length of 20 mm). A second incision was made over the knee, a medial parapatellar arthrotomy was then performed, and the patella was dislocated laterally with the knee in the extension position. The intercondylar notch was fully exposed, and the native ACL was then completely excised. Next, an electronic drill with an 18-gauge hypodermic needle was used to create bone tunnels at the intraarticular portion of the proximal tibia toward the distal femur, corresponding to the site of the anatomical attachment of the ACL. The tendon graft was passed through the tunnel, and both ends of the grafted tendon were secured to the surrounding periosteum using 4-0 ETHIBOND EXCEL® braided sutures (Ethicon, Somerville, NJ, USA). Subsequently, the rats were randomly allocated into three groups and received a local injection of IONP-Exos (100 μg/tunnel), BMSC-Exos (100 μg/tunnel), or PBS (Supplementary Fig. 1). The wounds were closed, and the animals were allowed ad libitum access to food and drinking water.

2.12. In vivo fluorescent labeling

Six rats were used for further exosome retention evaluation in vivo. Exosomes were incubated with DiR dye (Umibio, Shanghai, China) for 30 min at room temperature and centrifuged at 110,000 g for 70 min at 4 °C to remove the free dye. Then the DiR-labeled exosomes were injected into the bone tunnels. At 2 days after surgery, the IVIS Spectrum (Perkin Elmer, Waltham, MA, USA) was used to analyze the DiR-labeled exosome distribution.

2.13. Micro-CT analysis

The harvested specimens were scanned perpendicular to the long axis of the bone tunnels using a Skyscan 1276 micro-computed tomography (micro-CT) system (Bruker, Kontich, Belgium). The operating conditions for the X-ray tube were as follows: an X-ray tube potential of 85 kV, an X-ray tube current of 200 μA, and an exposure time of 384 ms. Reconstruction of the obtained data was accomplished by Nrecon (version 1.7.4.2). 3D images were obtained from contoured 2D images by methods based on distance transformation of the original grayscale images (CTVox version 3.3.0). 3D and 2D analyses were performed using the CT Analyzer software (version 1.18.8.0). The average cross-sectional bone tunnel areas were measured using ImageJ software, and the 3D reconstructed datasets were analyzed to obtain the trabecular bone volume fraction of the bone volume fraction (BV/TV), trabecular thickness (Tb. Th), trabecular number (Tb. N), trabecular separation (Tb. Sp), structure model index (SMI), bone mineral density (BMD), within the region of interest.

2.14. Biomechanical test

The femur-tendon graft-tibia complexes (FTGTC) were harvested at 4 weeks and 8 weeks after surgery and were stored at −80 °C until analysis. The specimens were thawed at 4 °C before being processed for biomechanical testing. According to previously published protocols [51–54], all soft tissue except the graft in the knee cavity and sutures at the tunnel exits was carefully removed to eliminate confounding factors before biomechanical testing. The shafts of the femur and tibia were firmly mounted on an electronic universal testing machine (AGS-X, Shimadzu, Kyoto, Japan), and the axis of distraction was adjusted to be parallel to the long axis of the tendon graft. For load-to-failure testing, specimens were preconditioned with 5 load cycles from 0 N to 0.5 N at a rate of 0.167 mm/s and then loaded to failure at the same rate. The failure load was recorded from the load-deformation curve, and the stiffness was calculated from the slope of the linear region of the curve. All tension tests were conducted at room temperature, and specimens were kept moistened with a saline solution throughout the testing period.

2.15. Histological and immunohistochemical analyses

After the micro-CT scan, the FTGTC samples were fixed in 4% neutral buffer formalin for 48 h and then decalcified with 10% EDTA for approximately 4 weeks. The samples were embedded with paraffin, and 5 μm-thick paraffin sections were obtained in the direction perpendicular to the longitudinal axis of the bone tunnel. The sections were stained with hematoxylin-eosin (H&E) and safranin O-Fast green (S&F) staining, and were visualized with inverted light microscopy (Nikon Co., Japan). Histomorphometric analysis was performed to assess the tendon-bone tunnel interface, the width of the tendon-bone interface, the percentage of graft-bone contact, and the healing pattern within the interface of the tendon-bone tunnel. Furthermore, immunohistochemical staining was performed to evaluate collagen formation and detect osteocalcin deposition. Sections were incubated with the associated primary antibodies overnight at 4 °C and subsequently incubated with the secondary antibodies for 1 h at room temperature. Then, the stained sections were developed in diaminobenzidine solution and counterstained with hematoxylin. Slides were observed, and digital images were captured using a Nikon light microscope equipped with a Nikon digital camera and NIS-Elements software (Nikon, Japan).

2.16. RNA selection and bioinformatics prediction

To identify potential exosomal miRNAs participating in the mechanisms underlying the stimulation of tendon-to-bone integration, based on previous miRNA expression profiles determined by high-throughput small RNA sequencing and a comprehensive literature review, several upregulated exosome-derived miRNAs (miR-21-5p, miR-25-3p, miR-92a-3p, miR-122-5p, miR-125b-5p, and miR-150-5p) were selected for further evaluation and pathway analysis [45,47,55–60]. The expression levels of miRNAs in exosomes were further validated using qRT-PCR.

Subsequently, the candidate target genes of miR-21-5p were predicted by the online tools TargetScan, picTar, miRanda, and miRWalk [61–66]. Kyoto Encyclopedia of Genes and Genomes (KEGG) pathway enrichment analysis was performed for candidate target genes related to fibrogenesis or osteogenesis. Next, the STRING [67] database (https://string-db.org/) was used to generate the protein-protein interactions of the selected target genes and import them into Cytoscape [68] to obtain hub genes. The expression of the top 10 hub genes was detected via the GEPIA database (http://gepia.cancer-pku.cn/index.html) (Supplementary Figs. 2 and 3).

2.17. Dual-luciferase reporter gene assay

The targeting relationship between miR-21-5p and SMAD7 was predicted through the biological prediction website and confirmed by dual-luciferase reporter gene assays. The wild type (WT) containing the predicted target site and the mutant type (MUT) without the binding site of SMAD7 to miR-21-5p were designed separately, amplified, and cloned into the pGL3 plasmid. HEK293 cells (5×10^4 cells/well) were seeded in 48-well plates, and luciferase reporter plasmids were transfected into the HEK293 cells with miR-NC or miR-21-5p mimics using Lipofectamine™ RNAiMAX (Invitrogen). After 24 h of transfection, the relative luciferase activity was measured by normalizing the firefly luminescence to the Renilla luminescence using the Dual-Luciferase Reporter Assay System (Promega, Madison, WI, USA) according to the manufacturer's protocol.

2.18. Cell transfection

For the overexpression or inhibition of miR-21-5p function, miR-21-5p mimics, miR-21-5p inhibitor, and appropriate negative controls (miR-NC or inhibitor-NC) were synthesized by RiboBio Technology Company (RiboBio Co, Ltd, Guangzhou, China). When NIH3T3 fibroblasts reached 60%–70% confluence, miR-21-5p mimics (100 nM), inhibitors (200 nM) or negative controls (100 nM) were transfected into NIH3T3 fibroblasts using Lipofectamine™ RNAiMAX (Invitrogen) in Opti-MEM (Invitrogen) according to the manufacturer's instructions. Overexpression of SMAD7 was achieved by transfecting cells with pcDNA-SMAD7 (GenePharma, Shanghai, China), and knockdown of SMAD7 was achieved by transfecting cells with siRNA-SMAD7 (GenePharma).

2.19. Statistical analysis

All experimental data are expressed as the mean ± standard deviation (SD). The Student's *t*-test was used to compare the data between two groups, and one-way analysis of variance (ANOVA) with Bonferroni post hoc tests was conducted to compare the data from multiple groups. Statistical analysis was conducted using Prism 8.0 software (GraphPad Software, Inc., CA, USA). All experiments were performed at least three times, and a *P*-value < 0.05 was considered statistically significant.

3. Results

3.1. IONPs characterization and cellular uptake

The magnetic actuate condition of BMSCs by adding IONPs in combination with SMF is shown in Fig. 1A. The surface charge of IONPs is shown in the zeta potential graph (Fig. 1B). The particles showed a negative zeta potential of approximately −57.50 mV, and the results obtained from ZetaView measurements showed that the size distributions of nanoparticles ranged from 90 to 120 nm (Fig. 1C). TEM images of BMSCs obtained 24 h after IONPs and SMF treatment showed that IONPs were well internalized into the cytoplasm of BMSCs (Fig. 1D). Prussian blue iron staining also showed that IONPs (20 μg/mL) were efficiently internalized into BMSCs and retained intracellularly, as IONPs were detected in BMSCs as blue-stained dots (Fig. 1E). For further exploration of the optimal magnetic actuated conditions, BMSCs were treated with IONPs at various concentrations ranging from 10 μg/mL to 120 μg/mL, and the CCK-8 assay showed that the IONPs did not exhibit cytotoxicity up to a concentration of 80 μg/mL, and 10–30 μg/mL promoted the growth and proliferation of BMSCs (Fig. 1F). To further explore the optimal stimulation conditions, we further treated BMSCs with different concentrations of IONPs (0, 10, 20, 30 μg/mL) in combination with different SMF strengths (0, 50, 100, and 200 mT). The results of the CCK-8 assay indicated that the optimal magnetically actuated system was a 20 μg/mL concentration of IONPs in combination with 100 mT SMF (Fig. 1G).

3.2. Exosome isolation, characterization, and internalization

IONP-Exos and BMSC-Exos were isolated and purified from the culture supernatant by differential ultracentrifugation (Fig. 2A). The results of western blot analysis confirmed that both IONP-Exos and BMSC-Exos expressed specific markers, including Hsp70, CD9, CD81, and TSG101, while the negative marker Calnexin was absent, as expected (Fig. 2B). NTA showed that the size of the exosomes mainly ranged from 80 to 160 nm, with a mean size of around 130 nm, and there was no distinguishing difference between exosomes derived from the two different conditions (Fig. 2C). Under TEM, exosomes appeared as round or oval vesicles with lipid bilayers, had a cup-like shape and a diameter of about 100 nm (Fig. 2D). No significant differences in size or shape were observed between the two types of exosomes. These features were consistent with previous studies, which indicated that the harvested vesicles were exosomes.

Exosomes were tracked in vitro after being labeled with PKH26 red fluorescent dye and were co-cultured with NIH3T3 fibroblasts, and the uptake of the fluorescent exosomes by the NIH3T3 fibroblasts was visualized using confocal microscopy (Fig. 2E). The normalized fluorescence intensity of the exosomes in NIH3T3 fibroblasts was time-dependent, and the fluorescence intensities were higher in the IONP-Exos group than in the BMSC-Exos group (Fig. 2F), suggesting that IONP-Exos were more effectively absorbed by NIH3T3 fibroblasts than BMSC-Exos.

3.3. IONP-Exos enhanced fibrogenesis in vitro

Fibroblast cell proliferation, migration, myofibroblast activation, and upregulated expression of profibrotic cytokines and extracellular matrix proteins are involved in the progression of tendon-to-bone integration. To measure the effect of IONP-Exos on NIH3T3 fibroblasts in detail, we first tested their effect on the proliferation capacity of NIH3T3 fibroblasts. Results from the CCK-8 assay demonstrated that the proliferation of NIH3T3 fibroblasts was significantly increased after treatment with the IONP-Exos and BMSC-Exos compared with the PBS group (Fig. 3A). Then, the effect of IONP-Exos on the migration capacity of NIH3T3 fibroblasts was tested. Results from the transwell assay demonstrated that the migration ability of NIH3T3 fibroblasts increases gradually for 24 h after treatment with the IONP-Exos and BMSC-Exos compared with the PBS group (Fig. 3B–D), and the scratch wound assay indicated that treatment of NIH3T3 fibroblasts with IONP-Exos and BMSC-Exos significantly enhanced their migration ability (Fig. 3E and F). Moreover, the expression levels of Col I, Col III, and α-SMA were upregulated at both the mRNA and protein levels in NIH3T3 fibroblasts treated with IONP-Exos and BMSC-Exos, as shown by qRT-PCR (Fig. 3G–I) and western blot analyses (Fig. 3J). These findings suggested that IONP-Exos and BMSC-Exos might promote tendon-to-bone healing by regulating the proliferation, migration, and fibrogenesis of fibroblasts.

3.4. IONP-Exos facilitated tendon-bone healing in a rat model

Local injection of biological therapy, such as PRP, is highly preferred in clinical practice as it is more direct and efficacious. Therefore, in this study, exosomes were also locally injected into the tendon-bone tunnel to test whether IONP-Exos could facilitate tendon-bone healing after ACLR in a rat model (Fig. 4A). As shown in the tracing study, we injected DiR-labeled IONP-Exos and BMSC-Exos during surgery, and the fluorescent results suggested that exosomes were retained in the surgical knee joints (Fig. 4B), which indicates low or no exosomes transfer, and the accumulation in the healing region might promote the tendon-bone healing process.

To quantitatively evaluate the effect of IONP-Exos and BMSC-Exos on the osteointegration quality of the tendon graft into the bone tunnels, we measured the mechanical properties of the tendon-bone interface within an earlier stage after ACLR. The failure modes after biomechanical analysis were simply divided into pullout from the bone tunnel or
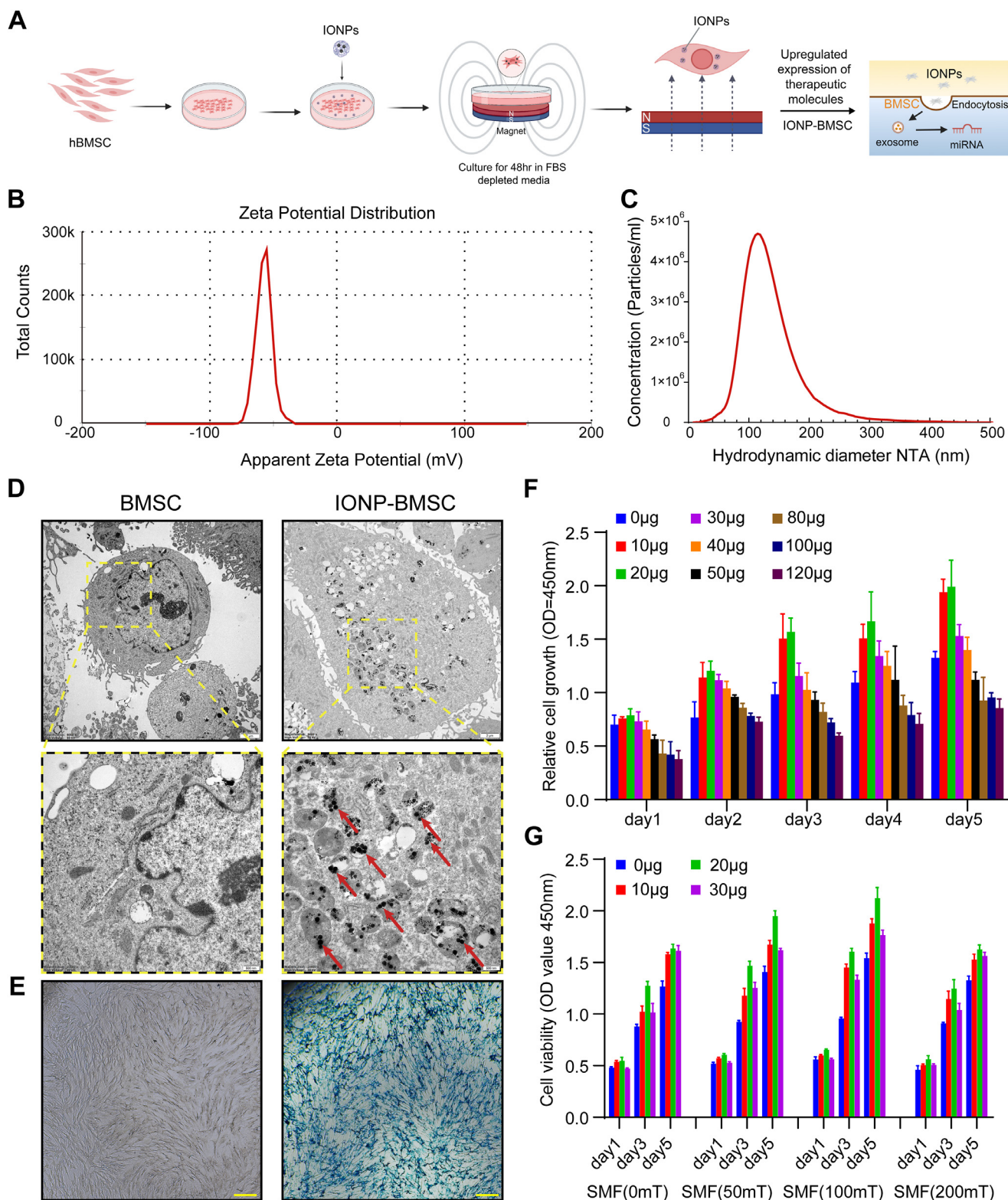
Fig. 1. IONPs characterization, cellular uptake of IONPs, and IONPs-SMF triggered cellular modification. (A) Schematic illustration of the preparation of IONP-SMF stimulated exosomes (IONP-Exos) derived from BMSCs that were triggered by IONPs in combination with SMF. (B) Zeta potential spectrum of IONPs dispersed in PBS at room temperature at a concentration of 1 mg/mL. (C) Size distribution of IONPs. (D) TEM image of IONPs (20 μg/mL) internalized by BMSCs. Red arrows indicate IONPs observed in the BMSC cytoplasm. (E) Compared with normal BMSCs, BMSCs incubated with IONPs (20 μg/mL) efficiently internalized IONPs and were stained using a Prussian blue iron staining kit. (F) Cell viability of BMSCs treated with various concentrations of IONPs and measured by CCK-8 assay. (G) Cell viability of BMSCs treated with the optimal concentrations of IONPs combined with different SMF strengths and measured by CCK-8 assay. IONPs: iron oxide nanoparticles; SMF: static magnetic field; TEM: transmission electron microscopy; BMSCs: bone mesenchymal stem cells; CCK-8: Cell Counting Kit-8. Each assay was performed in triplicate and/or carried out in at least three independent experiments; representative results are shown.
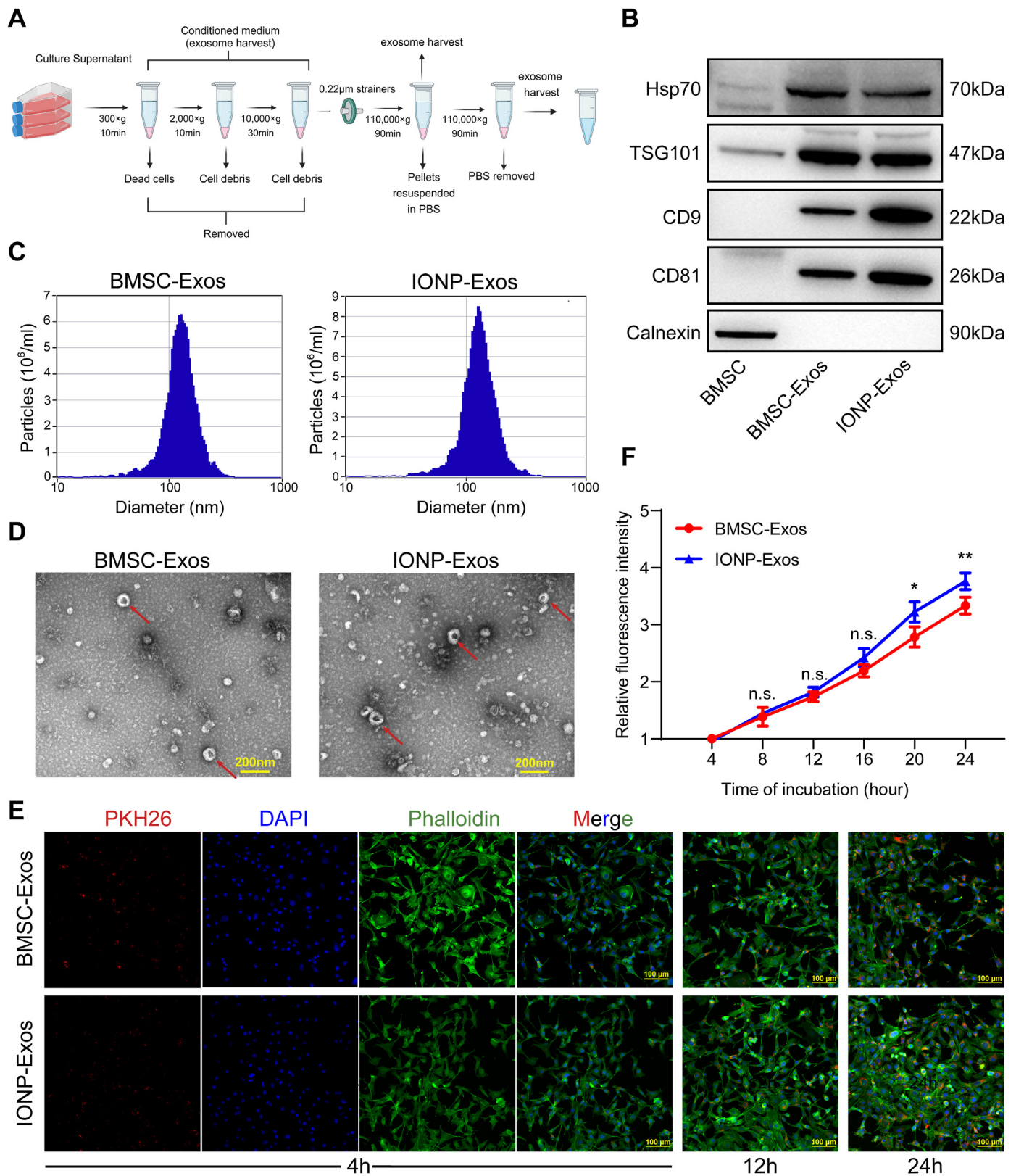
Fig. 2. Isolation, identification, and comparison of BMSC-Exos and IONP-Exos derived from BMSCs. (A) Schematic representation of the isolation and purification of exosomes by differential ultracentrifugation. All centrifugations were carried out at 4 °C. (B) Western blot analyses of specific surface markers, including Hsp70, CD9, CD81, TSG101, and the negative control calnexin. (C) NTA observation of the diameter distribution of isolated BMSC-Exos and IONP-Exos. (D) Representative image of BMSC-Exos and IONP-Exos observed under a transmission electron microscope. (E) Confocal images showed that the red fluorescence dye PKH26-labeled BMSC-Exos and IONP-Exos were endocytosed by NIH3T3 fibroblasts after 4 h, 12 h, and 24 h of incubation. F-actin was stained with phalloidin (green), and the nuclei were stained with DAPI (blue). (F) Comparison of the fluorescence intensities of BMSC-Exos and IONP-Exos at different time points. BMSC: bone mesenchymal stem cell; IONP: iron oxide nanoparticle; NTA: nanoparticle tracking analysis. Each assay was performed in triplicate and/or carried out in at least three independent experiments; representative results are shown. *$P < 0.05$; **$P < 0.01$; ***$P < 0.001$.
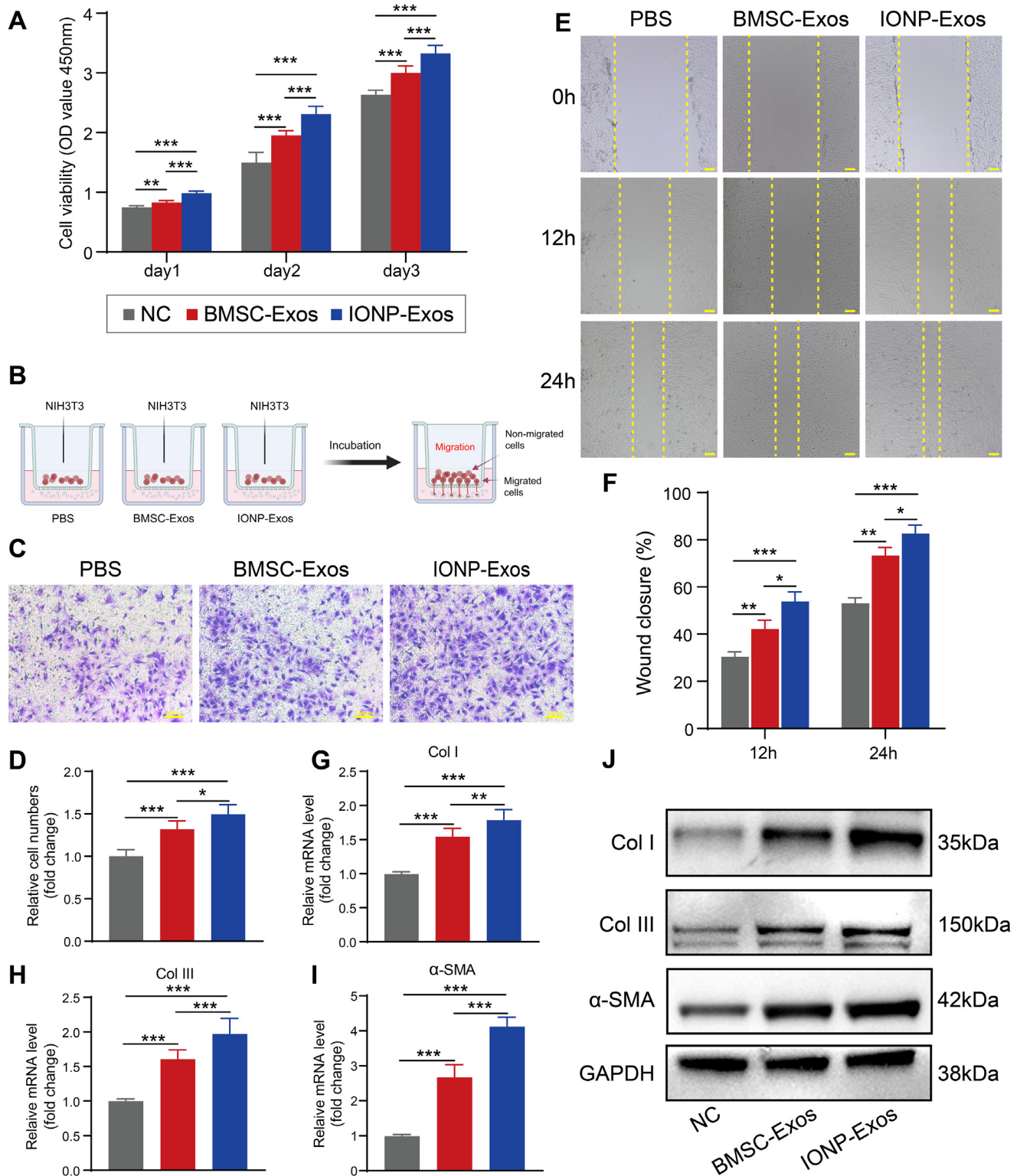
Fig. 3. IONP-Exos significantly promoted the proliferation, migration, and fibrogenesis of NIH3T3 fibroblasts. (A) IONP-Exos significantly promoted the proliferation of NIH3T3 fibroblasts, as demonstrated by the Cell Counting Kit-8 (CCK-8) assay. (B) Schematic illustration of the different parts of the transwell migration assay system. (C) IONP-Exos significantly promoted the migration of NIH3T3 fibroblasts as determined by the transwell assay after 24 h. (D) Quantitative analysis of the transwell assay. (E) IONP-Exos significantly promoted the migration ability of NIH3T3 fibroblasts as determined by the wound healing assay. (F) Quantitative analysis of the wound closure rates. (G–I) NIH3T3 fibroblasts were treated with IONP-Exos, BMSC-Exos, or PBS as the negative control, and the mRNA levels of Col I, Col III, and α-SMA were evaluated by qRT-PCR. (J) Western blot analysis of the expression of fibrotic-related proteins, including Col I, Col III, and α-SMA, GAPDH was used as a loading control. IONP: iron oxide nanoparticle; CCK-8: Cell Counting Kit-8; BMSC: bone mesenchymal stem cell. Each assay was performed in triplicate and/or carried out in at least three independent experiments; representative results are shown. *$P < 0.05$; **$P < 0.01$; ***$P < 0.001$. Scale bar: 100 μm.
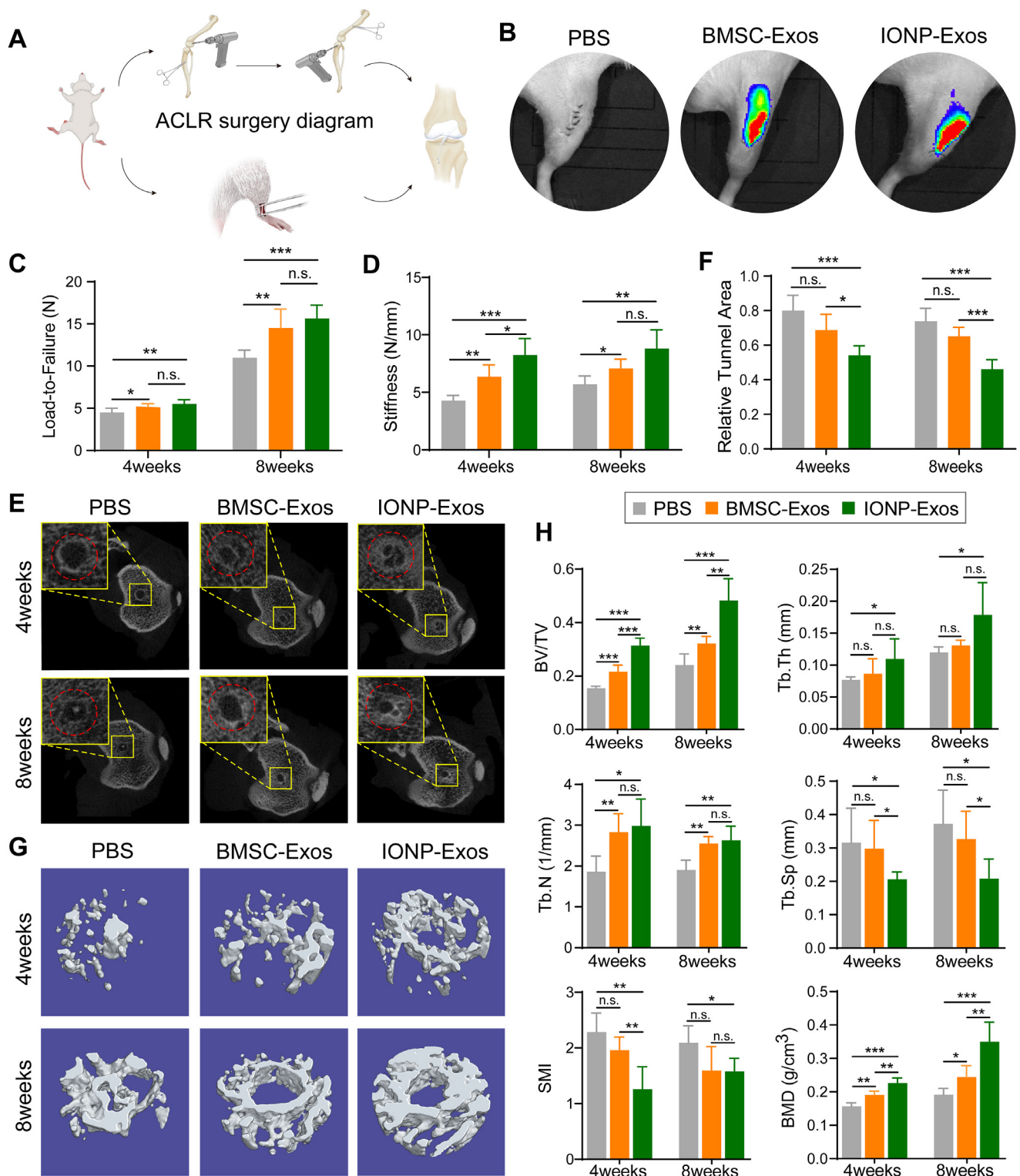
Fig. 4. Effects of exosomes on tendon-bone healing and the bone formation at the tendon-bone interface in a rat ALCR model. (A) Schematic representation of the ACLR surgical procedures in a rat ALCR model. (B) Representative IVIS images of the exosome retention in the surgical knee joints 48 h after local injection of IONP-Exos, BMSC-Exos, or PBS control into the bone tunnel. (C) The load-to-failure force of the femur-tendon graft-tibia complexes at 4 and 8 weeks after ACLR among the IONP-Exos, BMSC-Exos, or PBS groups. (D) Stiffness of the femur-tendon graft-tibia complexes at 4 weeks and 8 weeks after ACLR among the IONP-Exos injection, BMSC-Exos injection, and PBS injection groups. (E) Micro-CT images of the cross-sections of the tibial bone tunnels at 4 weeks and 8 weeks after ACLR. (F) Quantitative analysis of the cross-sectional bone tunnel area among the IONP-Exos, BMSC-Exos, and PBS groups. (G) Reconstructed 3-dimensional models of micro-CT images of newly formed bone at 4 weeks and 8 weeks after ACLR. (H) Quantitative results of new bone formation within the bone tunnel as measured by micro-CT at 4 weeks and 8 weeks after surgery. Micro-CT parameters: bone volume fraction (BV/TV); trabecular thickness (Tb. Th); trabecular number (Tb. N); trabecular separation (Tb. Sp); structure model index (SMI); bone mineral density (BMD). ACLR: anterior cruciate ligament reconstruction. micro-CT: micro-computed tomography. $*P < 0.05$; $**P < 0.01$; $***P < 0.001$.

ruptures outside the bone tunnel (at the midsubstance). At the 4-week time point, most tendon grafts failed by pullout from the bone tunnel (pullout/rupture: 7/1 grafts in the IONP-Exos group, 6/2 grafts in the BMSC-Exos group, and 6/2 grafts in the PBS group), while the graft failure location was more in the midsubstance (pullout/rupture: 2/6 grafts in the IONP-Exos group, 3/5 grafts in the BMSC-Exos group, and 4/4 grafts in the PBS group) at the 8-week time point. At both 4 and 8 weeks postoperatively, the maximal graft failure forces in the IONP-Exos and BMSC-Exos groups were significantly higher than those in the PBS group (Fig. 4C). Regarding the stiffness of the tendon graft, significantly higher stiffness of the FTGTC was detected in the IONP-Exos and BMSC-Exos groups (Fig. 4D). These results suggested that the healing quality at the tendon graft-bone interface was improved in the IONP-Exos and BMSC-Exos groups.

As for the tendon graft osseointegration process in vivo, typical images of the cross-sectional tibial bone tunnels at both 4 and 8 weeks after ACLR suggested more new bone ingrowth lining the bone tunnel in the IONP-Exos and BMSC-Exos groups (Fig. 4E), and quantitative analysis of the cross-sectional bone tunnel area also revealed that the tunnel areas in the IONP-Exos and BMSC-Exos groups were smaller than those in the PBS group (Fig. 4F). The 3D reconstructions of the peri-tunnel tissue further intuitively showed that more newly formed trabecular bone was found in the bone tunnel in the IONP-Exos and BMSC-Exos groups at both 4 and 8 weeks after ACLR (Fig. 4G). In addition, there were significant differences in BV/TV, Tb. Th, Tb. N, Tb. Sp, SMI, and BMD between the exosomes groups and the PBS group (Fig. 4H). These results from micro-CT analysis indicated that both IONP-Exos and BMSC-Exos significantly promoted the osteointegration of the tendon graft into the bone tunnel and prevented peri-tunnel bone loss.

Histological analysis at the tendon graft-bone interface was also conducted to evaluate the graft healing quality. The fibrous interface width at the tendon-bone interzone structure has been a negative factor affecting the tendon-bone healing quality [69], which was evaluated in this study. According to the H&E staining, an evident graft-bone interface was observed in all 3 groups at 2 weeks after ACLR surgery, followed by a distinct reduction in the width of the fibrous interface in all groups at 4 and 8 weeks after surgery (Fig. 5A) (Supplementary Fig. 4). At 2 weeks after surgery, there was disordered fibrovascular tissue at the tendon graft-bone interface; however, at 4 weeks after ACLR, large numbers of Sharpey's fibers (Fig. 5A, yellow arrows) formed in the interface, connecting the host bone and tendon graft, and at 8 weeks after ACLR, they continued to align into the surrounding bone tunnel. Compared with the PBS group, both the IONP-Exos and BMSC-Exos groups showed significantly narrower fibrous interface widths at 4 and 8 weeks after surgery, while no significant difference was observed in the fibrous interface width between the IONP-Exos and BMSC-Exos groups at 8 weeks after surgery (Fig. 5E). As indicated by S&F staining, only fibrous tissue formed at the interface in all three groups at 4 weeks after surgery, and the fibrocartilage zones were observed at the tendon-bone interface at 8 weeks after surgery in both the IONP-Exos and BMSC-Exos groups (Fig. 5B). A relatively larger fibrocartilage zone area was observed in the IONP-Exos group (Fig. 5G).

Furthermore, immunohistochemical staining was performed to evaluate the α-SMA and osteoid deposited at the tendon-bone interface. According to the immunohistochemical results, the expression of α-SMA in the IONP-Exos and BMSC-Exos groups was greater than that in the PBS groups at both 4 and 8 weeks after surgery (Fig. 5C and F). In addition, the expression of osteocalcin (OCN) in the IONP-Exos and BMSC-Exos groups was more significant than that in the PBS group (Fig. 5D and H). These findings indicated that collagen and osteoid deposition was more prominent in the IONP-Exos and BMSC-Exos groups, indicating that exosomes induced fibrogenesis and enhanced the graft osseointegration process.

3.5. Upregulated miR-21-5p expression in IONP-Exos promoted fibrogenesis in vitro

To further explore the key molecules that mediate the fibrogenic potential of the tendon graft-bone of IONP-Exos, we conducted qRT-PCR analysis to detect the levels of a class of miRNAs in IONP-Exos and BMSC-Exos, including miR-21-5p, miR-25-3p, miR-92a-3p, miR-122-5p, miR-125b-5p, and miR-150-5p, whose levels have been found to be markedly increased in IONP-Exos compared with BMSC-Exos, and have been reported to promote fibrogenesis [45,47,55–60]. The qRT-PCR data demonstrated that the expression level of miR-21-5p was much higher compared with other miRNAs (Fig. 6A). To further confirm that exosomal miR-21-5p can be transferred to NIH3T3 fibroblasts via IONP-Exos, miR-21-5p levels in NIH3T3 fibroblasts were measured after treatment with IONP-Exos or BMSC-Exos. According to the results, only mature miR-21 was upregulated in NIH3T3 fibroblasts, while there was no significant difference in pri-miR-21 or pre-miR-21 (Fig. 6B), suggesting that IONP-Exos containing exosomal miR-21-5p were internalized by NIH3T3 fibroblasts.

We hypothesized that exosomal miR-21-5p participated in the fibrogenic process by a paracrine mechanism, and NIH3T3 fibroblasts were transfected with either miR-21-5p mimics/inhibitor or negative control to address this issue. qRT-PCR analysis revealed a substantial increase in miR-21-5p expression levels after being transfected with miR-21-5p mimics, and significantly decreased miR-21-5p expression levels after transfected with miR-21-5p inhibitor, while transfection with miRNA-mimic NC and miRNA-inhibitor NC did not result in apparent changes in the miR-21-5p expression levels, as expected (Fig. 6C). Subsequent analysis of proliferation and migration was then initiated 24 h post-transfection. We found significant increases in proliferation and migration capacity compared to the control transfection group (Fig. 6D–G). Furthermore, overexpression of miR-21-5p also upregulated the expression of Col I, Col III, and a-SMA in NIH3T3 fibroblasts, at both the mRNA (Fig. 6H–J) and protein (Fig. 6K) levels. These in vitro transfection data indicated that increment in intracellular miR-21-5p stimulated NIH3T3 fibroblast proliferation and migration, and promoted an elevation in extracellular matrix (ECM) markers and fibrogenic markers.

3.6. Exosomal miR-21-5p regulates SMAD7 by targeting the 3′-UTR

MiRNAs regulate the gene expression of mRNA at the post-transcriptional level through transcript degradation or translational repression by binding to the 3′-untranslated region (UTR) of downstream target genes. To explore how miR-21-5p exerts its function in NIH3T3 fibroblasts, we utilized several bioinformatic target prediction algorithms to predict the target genes of miR-21-5p. SMAD7 was predicted and identified as a potential target of miR-21-5p, and a dual-luciferase reporter assay was performed for further confirmation.

Luciferase reporter constructs containing unaltered or mutated predicted miRNA-binding sites of SMAD7 (WT-SMAD7-3′UTR and MUT-SMAD7-3′UTR, respectively) were constructed and transfected with miR-21-5p mimics into NIH3T3 fibroblasts (Fig. 7A). Transfection of miR-21-5p mimics repressed the luciferase enzyme activity of the SMAD7 3′-UTR reporter gene, while MUT-SMAD7-3′UTR abolished this inhibition (Fig. 7B). In addition, the qRT-PCR assay demonstrated that the SMAD7 mRNA levels were significantly decreased in miR-21-5p mimics-transfected NIH3T3 fibroblasts, and western blot assays revealed that SMAD7 protein levels were decreased in NIH3T3 fibroblasts after transfection with miR-21-5p mimics (Fig. 7C and D). These results demonstrated that miR-21-5p mimics suppressed the SMAD7 mRNA and protein levels in NIH3T3 fibroblasts.

3.7. Exosomal miR-21-5p promoted fibrogenesis by targeting SMAD7

Our results confirmed that SMAD7 is a direct target of miR-21-5p, but whether exosomal miR-21-5p promotes fibrosis during tendon-bone
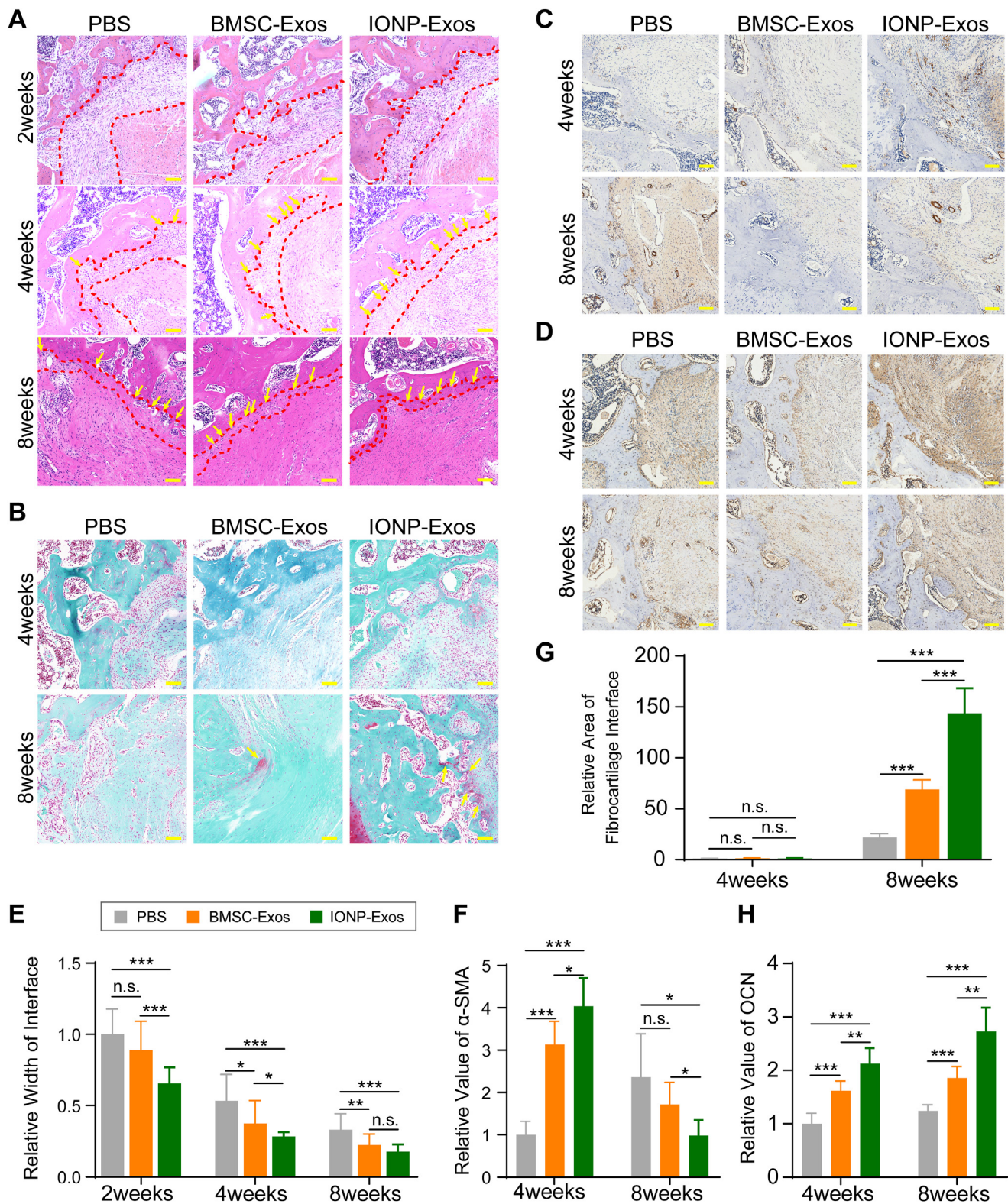
Fig. 5. IONP-Exos and BMSC-Exos improved histochemical performance in vivo. (A) Representative image of the tendon-bone interface by H&E staining at 4 weeks and 8 weeks postoperatively. The red irregular line outlines the tendon-bone interface, and the yellow arrows indicate Sharpey-like fibers. (B) Representative image of the tendon-bone interface by S&F staining at 4 weeks and 8 weeks postoperatively. S&F staining showed the presence of fibrocartilage tissues (yellow arrow) growing into the tendon-bone interface 8 weeks after surgery in the BMSC-Exos and IONP-Exos groups. (C) Immunohistochemical staining of α-smooth muscle actin (α-SMA) at the tendon-bone interface after ACLR at 4 and 8 weeks postoperatively. (D) Immunohistochemical staining of osteocalcin (OCN) at the tendon-bone interface after ACLR at 4 and 8 weeks postoperatively. (E) Quantitative analysis of the relative width of the tendon-bone interface. (F) Quantitative analysis of the relative area of fibrocartilage tissues of the regenerated enthesis at 4 and 8 weeks after surgery. (G) Quantitative analysis of the immunohistochemical staining of α-SMA. (H) Quantitative analysis of the immunohistochemical staining of OCN. H&E, hematoxylin-eosin; S&F, safranin O-Fast green; ALCR, anterior cruciate ligament reconstruction; IONP: iron oxide nanoparticle; BMSC: bone mesenchymal stem cell; SMF: static magnetic field. $*P < 0.05$; $**P < 0.01$; $***P < 0.001$.
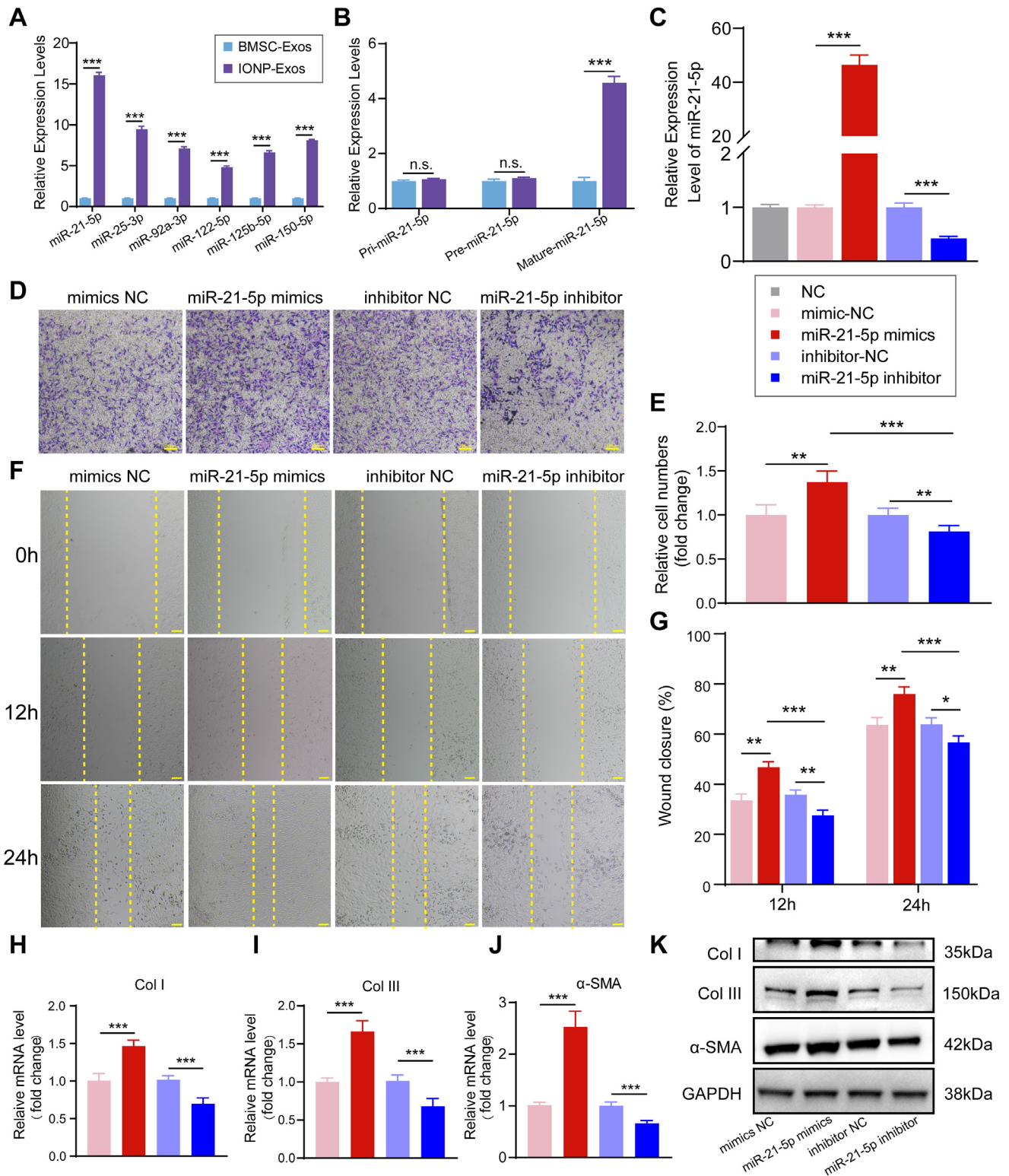
Fig. 6. miR-21-5p regulates the proliferation, migration, and fibrosis of NIH3T3 fibroblasts. (A) qRT-PCR analysis of the enrichment of the miRNAs in IONP-Exos and BMSC-Exos. (B) The expression levels of pri-miR-21, pre-miR-21, and mature-miR-21 in NIH3T3 fibroblasts after internalization of IONP-Exos and BMSC-Exos. (C) The transfection efficiency of miR-21-5p mimics into NIH3T3 fibroblasts was confirmed by qRT-PCR assay. (D) miR-21-5p mimics remarkably increased the migration of NIH3T3 fibroblasts as determined by the transwell assay. (E) Quantitative analysis of the transwell assay. (F) miR-21-5p mimics significantly promoted the migration ability of NIH3T3 fibroblasts as determined by the wound healing assay. (G) Quantitative analysis of the wound closure rates. (H–J) qRT-PCR showed that the mRNA levels of Col I, Col III, and α-SMA were upregulated after overexpression of miR-21-5p. (K) Western blot analysis showed that miR-21-5p mimics dramatically increased the protein expression of fibrotic markers, including Col I, Col III, and α-SMA. IONP: iron oxide nanoparticle; BMSC: bone mesenchymal stem cell. Each assay was performed in triplicate and/or carried out in at least three independent experiments; representative results are shown. *$P < 0.05$; **$P < 0.01$; ***$P < 0.001$. Scale bar: 100 μm.
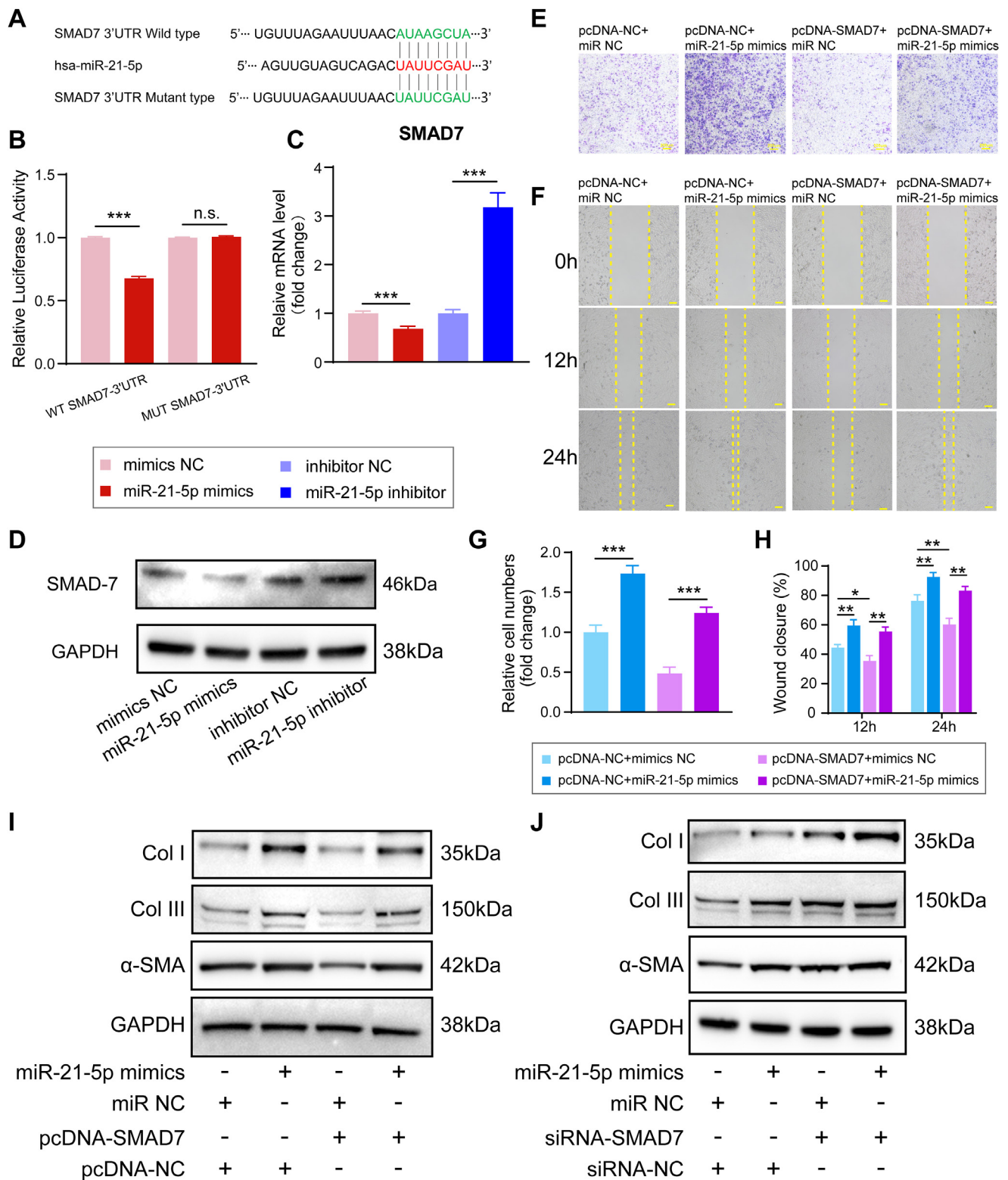
Fig. 7. Exosomal miR-21-5p derived from IONPs–incorporated BMSCs under SMF promotes fibrosis by regulating the downstream expression of genes in the SMAD7 pathway. (A) The predicted potential binding sites for miR-21-5p on the 3′-UTR of SMAD7. (B) A dual-luciferase reporter assay was performed to confirm that SMAD7 is the target gene of miR-21-5p. (C) qRT-PCR showed the SMAD7 expression levels after transfection of miR-21-5p mimics and inhibitor. (D) Western blot showing the SMAD7 expression levels after transfected with miR-21-5p mimics and inhibitor. (E) The transwell assay indicated that SMAD7 overexpression reversed the miR-21-5p mimics-induced increase in the migratory capacity of NIH3T3 fibroblasts. (F) The wound healing assay indicated that SMAD7 overexpression reversed the miR-21-5p mimics-induced increase in the migration capacity of NIH3T3 fibroblasts. (G) Quantitative analysis of the migration rate of NIH3T3 fibroblasts. (H) Quantitative analysis of the wound closure rates. (I) Western blot assay indicated that the overexpression of SMAD7 suppressed the upregulation of Col I, Col III, and α-SMA protein expression induced by the miR-21-5p mimics. (J) Western blot assay indicated that suppression of SMAD7 promoted the upregulation of Col I, Col III, and α-SMA protein expression induced by the miR-21-5p mimics. IONP: iron oxide nanoparticle; BMSC: bone mesenchymal stem cell. Each assay was performed in triplicate and/or carried out in at least three independent experiments; representative results are shown. $*P < 0.05$; $**P < 0.01$; $***P < 0.001$. Scale bar: 100 μm.

healing by regulating SMAD7 expression needs further investigation. According to the manufacturers' instructions, NIH3T3 fibroblasts were co-transfected with the SMAD7 overexpression vector (pcDNA-SMAD7) or empty vector (pcDNA-NC) and miR-21-5p mimics or mimics NC. Transwell and wound healing assays indicated that the SMAD7 over-expression effectively counteracted the increase in migratory capacity induced by miR-21-5p mimics (Fig. 7E–H). In addition, western blot analysis results indicated that the upregulation of Col I, Col III, and α-SMA protein expression induced by the miR-21-5p mimics was reversed in the pcDNA-SMAD7+miR-21-5p mimics group (Fig. 7I). Finally, to further confirm the role of SMAD7 in exosomal miR-21-5p induced tendon-bone healing, NIH3T3 fibroblasts were co-transfected with siRNA-SMAD7 or siRNA-NC (scrambled or non-targeting) and miR-21-5p mimics or mimics NC. Western blot analysis revealed that the upregulations of Col I, Col III, and α-SMA protein expression induced by the miR-21-5p mimics was further promoted by suppression of SMAD7 (Fig. 7J). Taken together, these findings confirmed the hypothesis that exosomal miR-21-5p promotes fibrogenesis in tendon-bone healing by downregulating the expression of SMAD7. Collectively, our results indicate that exosomes derived from IONP-incorporated BMSCs under SMF conditions, containing high-abundance miRNAs, such as miR-21-5p, could promote fibrosis by upregulating the functional activity of

fibroblasts and facilitating tendon graft-bone healing. The proposed underlying mechanism by which IONP-Exos promote tendon-bone healing is presented in Fig. 8.

4. Discussion

Insufficient tendon graft-bone integration has been widely recognized as one of the major causes of early failure after ACLR. Thus, a lot of research investigated biological interventions that may promote tendon graft-bone incorporation and facilitate aggressive rehabilitation and a faster return to physical activity [15,70–72]. Currently, there is a lack of research concerning the mechanism of exosomes in tendon-bone healing, and this is the first study, to the best of our knowledge, to investigate the effects of exosomes on tendon-bone integration in an ACLR model. In this study, IONP-Exos, a novel type of exosome derived from magnetically actuated BMSCs, showed enhanced therapeutic potential for tendon-bone integration and were successfully developed and fabricated. Our data further indicate that (i) there was no significant difference in characterization between IONP-Exos and BMSC-Exos; (ii) IONP-Exos were efficiently internalized by NIH3T3 fibroblasts and significantly promoted the proliferation and migration abilities of NIH3T3 fibroblasts; (iii) in vivo study results demonstrated that local injection of IONP-Exos
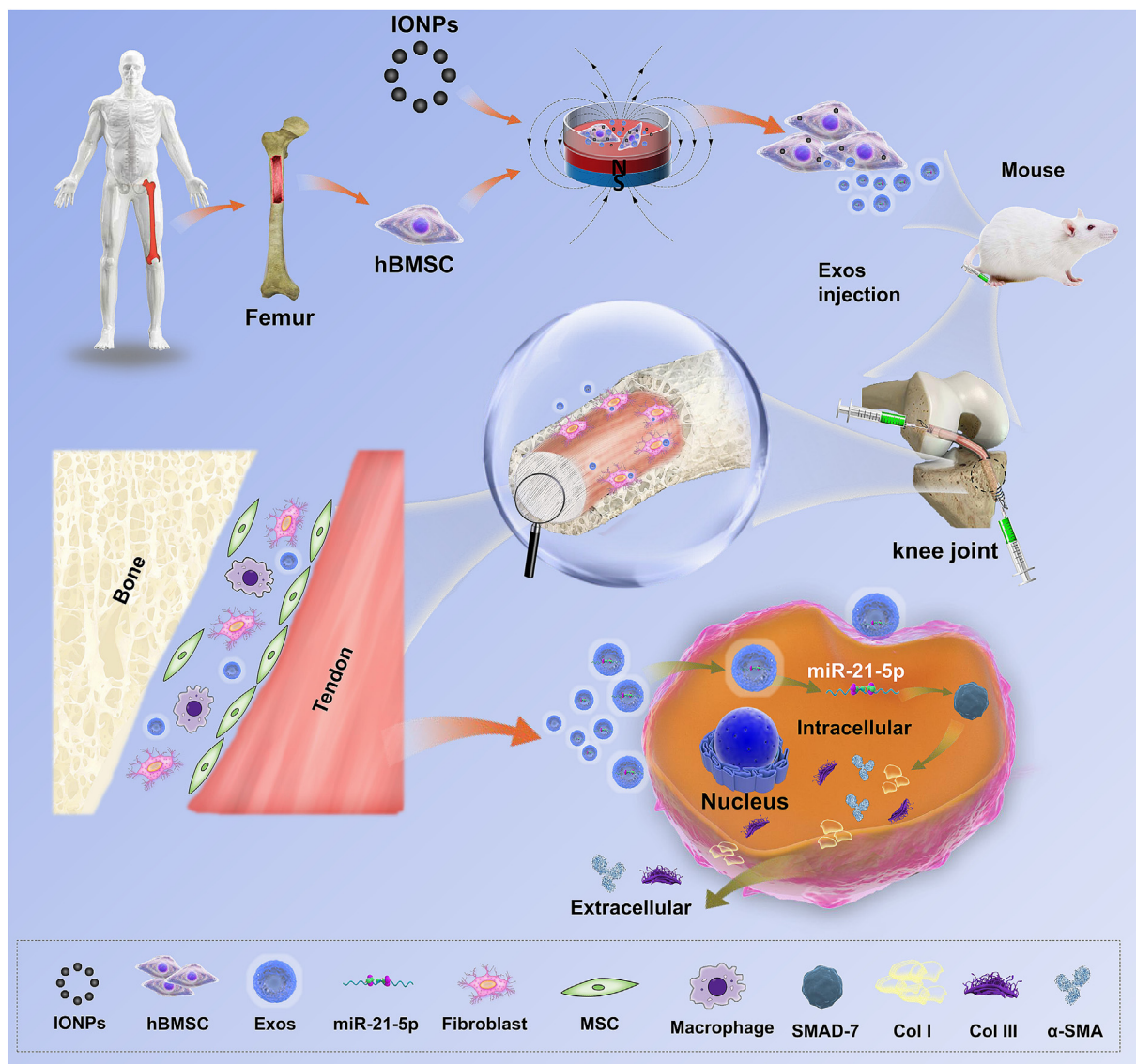

Fig. 8. The underlying mechanism by which IONP-Exos promoted tendon-to-bone integration.

can effectively enhance tendon-bone integration via mechanical, radiological, and histological measurements in a rat ACLR model; (iv) exosomal miR-21-5p was found to be enriched in IONP-Exos and miR-21-5p mimics enhanced the proliferation and migration capacities of NIH3T3 fibroblasts; and (v) exosomal miR-21-5p promoted fibrogenesis and enhanced tendon-bone integration by reducing SMAD7 expression levels. Collectively, our findings confirmed the hypothesis that exosomes derived from IONPs-incorporated BMSCs under SMF exhibited better therapeutic efficacy in tendon-bone integration.

We also focused on the mechanisms by which IONP-Exos promote tendon-bone integration. The findings of this study suggested that there were significant differences in the cellular behavior of BMSCs after magnetic stimulation with IONPs and SMF. The IONPs, which interact with the magnetic force, may be sensed by the BMSCs and lead to biochemical changes at the cellular, molecular and genetic levels, further altering the composition of the secreted exosomes both transcriptomically and proteomically [73]. Previous studies have demonstrated that IONPs and SMF stimulation could induce upregulated expression of the therapeutic molecules, and these molecules with upregulated expression were also retained in IONP-Exos, which were relatively higher in IONP-Exos than in normal exosomes [43,73]. Although the exact mechanisms of the upregulated expression of molecules such as miRNAs in IONP-Exos remain unknown, many molecules are already known to be involved in anti-apoptotic, anti-inflammatory, and proangiogenic processes [74].

The profibrotic effect of IONP-Exos was mainly explored in this study, and we found that IONP-Exos deeply affect cellular behaviors and modulate the phenotype of fibroblasts. Our findings were consistent with a previous study, which found that exosomal miR-21-5p derived from BMSCs directly targets SMAD7 and leads to activation of fibrogenesis and tendon adhesion after tendon injury [56]. Exosomal miR-21-5p stimulates fibroblasts to differentiate into myofibroblasts, which overexpress α-SMA, overproduce ECM and fibrogenic markers [56]. As a consequence of local IONP-Exos injections, myofibroblasts are enriched, and the ECM accumulates at the tendon-bone interface, promoting tendon-bone integration.

In general, peri-tunnel bone loss after ACLR is commonly observed in both clinical and pre-clinical studies, which might adversely affect the tendon graft enthesis mineralization and result in a less stable surface for tendon-bone integration [75,76]. Based on previous studies, SMF or IONPs, delivered alone or in combination, could enhance osteogenesis, inhibit osteoclastogenesis, and enhance the stability of the bone tunnel healing surface [45–47,49,77,78]. Our study also found that IONP-Exos improved bone tunnel healing by decreasing the bone tunnel diameter and stimulating new trabecular bone formation. More essentially, the complex interlocking between fibrocartilage and bone tunnel surface contributes to the mechanical strength of the tendon-bone integration, and fibrocartilage was formed at the tendon-bone interface in the IONP-Exos group, while only a fibrous interface was observed in the PBS group at 8 weeks after surgery [79]. Therefore, fibrocartilage at the tendon-bone interzone structure also leads to better biomechanical performance after IONP-Exos interventions.

Angiogenesis, a process of new blood vessel formation from the pre-existing vasculature, is another essential process, as increased vascularization around the tendon-bone interface is essential for tendon revascularization and new bone formation [80–82]. Huang et al. explored the role of BMSC-derived exosomes in tendon-bone healing after rotator cuff repair in a rat model and found that BMSC-derived exosomes promote tendon-bone healing by promoting angiogenesis and inhibiting inflammation [83]. Although the proangiogenic effect was not investigated in this study, IONP-Exos probably also induced angiogenesis and promoted tendon-bone interface regeneration [45,47,83].

Regarding the mechanism of exosomes, exosomal miRNAs have been established as key regulators of multitudinous cellular processes with fundamental roles in regenerative tissue repair. Therefore, miRNA

therapies might be a new molecular intervention and a promising approach to improving tendon-bone healing and other tissue regeneration [84]. In this study, we further explored miRNAs that may be associated with tendon-bone integration, and revealed that miR-21-5p was significantly enriched in IONP-Exos, which could be transferred into NIH3T3 fibroblasts and play a vital role in the complex biological processes involved in the tendon-bone integration. Several previous studies have reported that miR-21 could regulate the expression of collagens and other ECM components, and our findings further broaden the current understanding of the mechanism of miR-21-5p overexpression in tendon-bone healing, revealing that exosomal miR-21-5p acts as an essential inducer of profibrotic protein expression on the tendon-bone tunnel surface [85,86].

To investigate the mechanisms underlying miR-21-5p-induced fibrogenesis in the tendon-bone tunnel surface, we selected SMAD7 as a candidate gene. Studies have shown that the TGF-β/SMAD signaling pathway contributes to the tendon repair and adhesions [87–89]. TGF-β is a multi-functional mediator that regulates proliferation, differentiation, apoptosis, adhesion, and migration in various cells, and TGF-β1 is considered a crucial mediator of tissue fibrosis [90,91]. TGF-β1 exerts its biological effects by activating downstream mediators, including SMAD2 and SMAD3, which are negatively regulated by SMAD7 expression. SMAD2 and SMAD3 participate in the transcription of downstream profibrotic target genes, while SMAD7 negatively regulates the TGF-β/SMAD signaling pathway and reduces TGF-β1-mediated fibrosis [91,92]. The in vitro data suggested that IONP-Exos were enriched in miR-21-5p, and exosomal miR-21-5p could downregulate SMAD7 expression and activate the TGF-β/SMAD-dependent pathway, which further promoted ECM production and tissue fibrosis in tendon-bone healing.

This proof-of-concept study also has some limitations. First, we evaluated the in vivo tendon-bone healing at 4 and 8 weeks after surgery according to previous studies, which is a relatively short monitoring period [24,54]. Second, the effect of IONP-Exos on angiogenesis was not explored in vitro, but has been fully elucidated in previous studies [45, 47]. The vascular networks at the tendon-bone tunnel surface were not assessed by angiography, mainly due to the relatively small diameter of the bone tunnel. Third, the effect of IONP-Exos on osteogenesis was also not explored in vitro, as there are consistent reports concerning this issue [47,78]. Finally, additional studies will be needed to address the exact mechanisms by which IONPs in combination with SMF lead to the upregulation of miRNAs in IONP-Exos.

5. Conclusion

The present study demonstrates that therapeutic molecule-enriched IONP-Exos can improve tendon-bone integration, which could be a promising therapeutic strategy to enhance tendon-bone healing after ACLR. We further confirmed that the specific exosomal cargo miR-21-5p was significantly increased, which further regulated SMAD7 expression and promoted tendon-bone integration. Altogether, these findings suggested that IONP-Exos may be an effective cell-free therapy that can replace BMSC therapy for the promotion of tendon-bone healing, which opens new avenues in pre-clinical and clinical research.

Declaration of competing interest

The authors declare that they have no known competing financial interests or personal relationships that could have appeared to influence the work reported in this paper.

Appendix A. Supplementary data

Supplementary data to this article can be found online at https://doi.org/10.1016/j.mtbio.2022.100319.

References

[1] E. Mashkovskiy, J.M. Beverly, U. Stöcker, S. Bychkovskiy, Ice climbing festival in Sochi 2014 Winter Olympics: medical management and injury analysis, Wilderness Environ. Med. 27 (1) (2016) 117–124.

[2] S.-N. Pan, X.-H. Lyu, Q. Liu, Q.-Y. Guo, Pay attention to the imaging study of sport injury and illness in winter olympics sports, Chin. Med.J. (Engl.) 131 (2018) 1013–1015.

[3] D.A. Lewis, B. Kirkbride, C.J. Vertullo, L. Gordon, T.A. Comans, Comparison of four alternative national universal anterior cruciate ligament injury prevention programme implementation strategies to reduce secondary future medical costs, Br. J. Sports Med. 52 (4) (2018) 277–282.

[4] L.S. Lohmander, P.M. Englund, L.L. Dahl, E.M. Roos, The long-term consequence of anterior cruciate ligament and meniscus injuries: osteoarthritis, Am. J. Sports Med. 35 (10) (2007) 1756–1769.

[5] T. Grøntvedt, L. Engebretsen, P. Benum, O. Fasting, A. Mølster, T. Strand, A prospective, randomized study of three operations for acute rupture of the anterior cruciate ligament. Five-year follow-up of one hundred and thirty-one patients, J. Bone Joint Surg. Am. 78 (2) (1996) 159–169.

[6] M. Group, Effect of graft choice on the outcome of revision anterior cruciate ligament reconstruction in the Multicenter ACL Revision Study (MARS) Cohort, Am. J. Sports Med. 42 (10) (2014) 2301–2310.

[7] L.V. Gulotta, S.A. Rodeo, Biology of autograft and allograft healing in anterior cruciate ligament reconstruction, Clin. Sports Med. 26 (4) (2007) 509–524.

[8] Region, and segment forecasts, cruciate ligament repair procedures market size, share & trends analysis report by procedure type (anterior cruciate ligament repair, posterior cruciate ligament repair). Available at: https://www.grandviewresearch.com/industry-analysis/cruciate-ligament-repair-procedures-market (accessed on June 05, 2022).

[9] A.L. Gornitzky, A. Lott, J.L. Yellin, P.D. Fabricant, J.T. Lawrence, T.J. Ganley, Sport-specific yearly risk and incidence of anterior cruciate ligament tears in high school athletes: a systematic review and meta-analysis, Am. J. Sports Med. 44 (10) (2016) 2716–2723.

[10] P. Di Benedetto, E. Di Benedetto, A. Fiocchi, A. Beltrame, A. Causero, Causes of failure of anterior cruciate ligament reconstruction and revision surgical strategies, Knee Surg. Relat. Res. 28 (4) (2016) 319.

[11] S. Pache, J. Del Castillo, G. Moatshe, R.F. LaPrade, Anterior cruciate ligament reconstruction failure and revision surgery: current concepts, J. ISAKOS: Joint Disord. Orthop. Sports Med. 5 (6) (2020) 351–358.

[12] G. Samitier, A.I. Marcano, E. Alentorn-Geli, R. Cugat, K.W. Farmer, M.W. Moser, Failure of anterior cruciate ligament reconstruction, Arch. Bone Jt. Surg. 3 (4) (2015) 220.

[13] C.R. Chu, A.A. Williams, Quantitative MRI UTE-T2* and T2* show progressive and continued graft maturation over 2 years in human patients after anterior cruciate ligament reconstruction, Orthop. J. Sports Med. 7 (8) (2019), 2325967119863056.

[14] A. Hexter, T. Thangarajah, G. Blunn, F. Haddad, Biological augmentation of graft healing in anterior cruciate ligament reconstruction: a systematic review, Bone Joint Lett. J 100 (3) (2018) 271–284.

[15] H. Li, S. Chen, H. Tao, H. Li, S. Chen, Correlation analysis of potential factors influencing graft maturity after anterior cruciate ligament reconstruction, Orthop. J. Sports Med. 2 (10) (2014), 2325967114553552.

[16] S.U. Scheffler, F.N. Unterhauser, A. Weiler, Graft remodeling and ligamentization after cruciate ligament reconstruction, Knee Surg. Sports Traumatol. Arthrosc. 16 (9) (2008) 834–842.

[17] S. Yao, P.S.H. Yung, P.P.Y. Lui, Tackling the challenges of graft healing after anterior cruciate ligament reconstruction—thinking from the endpoint, Front. Bioeng. Biotechnol. 9 (2021), 756930.

[18] F. Bi, Y. Chen, J. Liu, Y. Wang, D. Xu, K. Tian, Anterior cruciate ligament reconstruction in a rabbit model using a silk-collagen scaffold modified by hydroxyapatite at both ends: a histological and biomechanical study, J. Orthop. Surg. Res. 16 (1) (2021) 1–12.

[19] M.S. Davey, E.T. Hurley, D. Withers, R. Moran, C.J. Moran, Anterior cruciate ligament reconstruction with platelet-rich plasma: a systematic review of randomized control trials, Arthroscopy 36 (4) (2020) 1204–1210.

[20] Y.-M. Huang, C.-C. Huang, P.-I. Tsai, K.-Y. Yang, S.-I. Huang, H.-H. Shen, H.-J. Lai, S.-W. Huang, S.-Y. Chen, F.-H. Lin, Three-dimensional printed porous titanium screw with bioactive surface modification for bone–tendon healing: a rabbit animal model, Int. J. Mol. Sci. 21 (10) (2020) 3628.

[21] C.-C. Lu, C.-J. Ho, H.-T. Huang, S.-Y. Lin, S.-H. Chou, P.-H. Chou, M.-L. Ho, Y.-C. Tien, Effect of freshly isolated bone marrow mononuclear cells and cultured bone marrow stromal cells in graft cell repopulation and tendon-bone healing after allograft anterior cruciate ligament reconstruction, Int. J. Mol. Sci. 22 (6) (2021) 2791.

[22] P.Y. Mengsteab, T. Otsuka, A. McClinton, N.S. Shemshaki, S. Shah, H.-M. Kan, E. Obopilwe, A.T. Vella, L.S. Nair, C.T. Laurencin, Mechanically superior matrices promote osteointegration and regeneration of anterior cruciate ligament tissue in rabbits, Proc. Natl. Acad. Sci. U. S. A. 117 (46) (2020) 28655–28666.

[23] T. Pesqueira, R. Costa-Almeida, M.E. Gomes, Uncovering the effect of low-frequency static magnetic field on tendon-derived cells: from mechanosensing to tenogenesis, Sci. Rep. 7 (1) (2017) 1–12.

[24] Y. Sun, W. Chen, Y. Hao, X. Gu, X. Liu, J. Cai, S. Liu, J. Chen, S. Chen, Stem cell–conditioned medium promotes graft remodeling of midsubstance and intratunnel incorporation after anterior cruciate ligament reconstruction in a rat model, Am. J. Sports Med. 47 (10) (2019) 2327–2337.

[25] B. Wei, C. Wang, C. Yan, B. Tang, X. Yu, H. Zhang, L. Tang, Q. Wang, Osteoprotegerin/bone morphogenetic protein 2 combining with collagen sponges on tendon-bone healing in rabbits, J. Bone Miner. Metabol. 38 (4) (2020) 432–441.

[26] P. Zhang, F. Han, T. Chen, Z. Wu, S. Chen, Swiss roll"-like bioactive hybrid scaffolds for promoting bone tissue ingrowth and tendon-bone healing after anterior cruciate ligament reconstruction, Biomater. Sci. 8 (3) (2020) 871–883.

[27] R. Guo, L. Gao, B. Xu, Current evidence of adult stem cells to enhance anterior cruciate ligament treatment: a systematic review of animal trials, Arthroscopy 34 (1) (2018) 331–340, e332.

[28] P.P.Y. Lui, O.T. Wong, Y.W. Lee, Application of tendon-derived stem cell sheet for the promotion of graft healing in anterior cruciate ligament reconstruction, Am. J. Sports Med. 42 (3) (2014) 681–689.

[29] T. Matsumoto, Y. Sato, T. Kobayashi, K. Suzuki, A. Kimura, T. Soma, E. Ito, T. Kikuchi, S. Kobayashi, K. Harato, Adipose-derived stem cell sheets improve early biomechanical graft strength in rabbits after anterior cruciate ligament reconstruction, Am. J. Sports Med. 49 (13) (2021) 3508–3518.

[30] C.A. Herberts, M.S. Kwa, H.P. Hermsen, Risk factors in the development of stem cell therapy, J. Transl. Med. 9 (1) (2011) 1–14.

[31] P.W. Marks, C.M. Witten, R.M. Califf, Clarifying stem-cell therapy's benefits and risks, N. Engl. J. Med. 376 (11) (2017) 1007–1009.

[32] T.M. Sissung, W.D. Figg, Stem cell clinics: risk of proliferation, Lancet Oncol. 21 (2) (2020) 205–206.

[33] M. Mittelbrunn, F. Sánchez-Madrid, Intercellular communication: diverse structures for exchange of genetic information, Nat. Rev. Mol. Cell Biol. 13 (5) (2012) 328–335.

[34] S. El Andaloussi, I. Mäger, X.O. Breakefield, M.J. Wood, Extracellular vesicles: biology and emerging therapeutic opportunities, Nat. Rev. Drug Discov. 12 (5) (2013) 347–357.

[35] M. Yáñez-Mó, P.R.-M. Siljander, Z. Andreu, A. Bedina Zavec, F.E. Borràs, E.I. Buzas, K. Buzas, E. Casal, F. Cappello, J. Carvalho, Biological properties of extracellular vesicles and their physiological functions, J. Extracell. Vesicles 4 (1) (2015), 27066.

[36] D.G. Phinney, M.F. Pittenger, Concise review: MSC-derived exosomes for cell-free therapy, Stem Cell. 35 (4) (2017) 851–858.

[37] Y. Wang, G. He, Y. Guo, H. Tang, Y. Shi, X. Bian, M. Zhu, X. Kang, M. Zhou, J. Lyu, Exosomes from tendon stem cells promote injury tendon healing through balancing synthesis and degradation of the tendon extracellular matrix, J. Cell Mol. Med. 23 (8) (2019) 5475–5485.

[38] Z. Yao, J. Li, H. Xiong, H. Cui, J. Ning, S. Wang, X. Ouyang, Y. Qian, C. Fan, MicroRNA engineered umbilical cord stem cell-derived exosomes direct tendon regeneration by mTOR signaling, J. Nanobiotechnol. 19 (1) (2021) 1–18.

[39] M. Zhang, H. Liu, Q. Cui, P. Han, S. Yang, M. Shi, T. Zhang, Z. Zhang, Z. Li, Tendon stem cell-derived exosomes regulate inflammation and promote the high-quality healing of injured tendon, Stem Cell Res. Ther. 11 (1) (2020) 1–15.

[40] P.P.-Y. Lui, P. Zhang, K.-M. Chan, L. Qin, Biology and augmentation of tendon-bone insertion repair, J. Orthop. Surg. Res. 5 (1) (2010) 1–14.

[41] A. Vinhas, M.T. Rodrigues, A. Gonçalves, R. Reis, M.E. Gomes, Magnetic responsive materials modulate the inflammatory profile of IL-1β conditioned tendon cells, Acta Biomater. 117 (2020) 235–245.

[42] A. Vinhas, M.T. Rodrigues, A.I. Gonçalves, R.L. Reis, M.E. Gomes, Pulsed electromagnetic field modulates tendon cells response in il-1β-conditioned environment, J. Orthop. Res. 38 (1) (2020) 160–172.

[43] S. Hao, Y. Zhang, J. Meng, J. Liu, T. Wen, N. Gu, H. Xu, Integration of a superparamagnetic scaffold and magnetic field to enhance the wound-healing phenotype of fibroblasts, ACS Appl. Mater. Interfaces 10 (27) (2018) 22913–22923.

[44] Y. Xia, J. Sun, L. Zhao, F. Zhang, X.J. Liang, Y. Guo, M.D. Weir, M.A. Reynolds, N. Gu, H.H.K. Xu, Magnetic field and nano-scaffolds with stem cells to enhance bone regeneration, Biomaterials 183 (2018) 151–170.

[45] L.K. Di Wu, J. Tian, Y. Wu, J. Liu, Z. Li, X. Wu, Y. Huang, B. Gao, H. Wang, Z. Wu, Exosomes derived from bone mesenchymal stem cells with the stimulation of Fe3O4 nanoparticles and static magnetic field enhance wound healing through upregulated miR-21-5p, Int. J. Nanomed. 15 (2020) 7979.

[46] Y. He, L. Yu, J. Liu, Y. Li, Y. Wu, Z. Huang, D. Wu, H. Wang, Z. Wu, G. Qiu, Enhanced osteogenic differentiation of human bone–derived mesenchymal stem cells in 3-dimensional printed porous titanium scaffolds by static magnetic field through up-regulating Smad4, Faseb. J. 33 (5) (2019) 6069–6081.

[47] D. Wu, X. Chang, J. Tian, L. Kang, Y. Wu, J. Liu, X. Wu, Y. Huang, B. Gao, H. Wang, Bone mesenchymal stem cells stimulation by magnetic nanoparticles and a static magnetic field: release of exosomal miR-1260a improves osteogenesis and angiogenesis, J. Nanobiotechnol. 19 (1) (2021) 1–19.

[48] N. Percie du Sert, V. Hurst, A. Ahluwalia, S. Alam, M.T. Avey, M. Baker, W.J. Browne, A. Clark, I.C. Cuthill, U. Dirnagl, M. Emerson, P. Garner, S.T. Holgate, D.W. Howells, N.A. Karp, S.E. Lazic, K. Lidster, C.J. MacCallum, M. Macleod, E.J. Pearl, O.H. Petersen, F. Rawle, P. Reynolds, K. Rooney, E.S. Sena, S.D. Silberberg, T. Steckler, H. Würbel, The ARRIVE guidelines 2.0: updated guidelines for reporting animal research, PLoS Biol. 18 (7) (2020), e3000410.

[49] V. Martinek, C. Latterman, A. Usas, S. Abramowitch, S.L. Woo, F.H. Fu, J. Huard, Enhancement of tendon-bone integration of anterior cruciate ligament grafts with bone morphogenetic protein-2 gene transfer: a histological and biomechanical study, J. Bone Joint Surg. Am. 84 (7) (2002) 1123–1131.

[50] Y. Mifune, T. Matsumoto, K. Takayama, S. Terada, N. Sekiya, R. Kuroda, M. Kurosaka, F.H. Fu, J. Huard, Tendon graft revitalization using adult anterior cruciate ligament (ACL)-derived CD34+ cell sheets for ACL reconstruction, Biomaterials 34 (22) (2013) 5476–5487.

[51] H. Li, J. Li, J. Jiang, F. Lv, J. Chang, S. Chen, C. Wu, An osteogenesis/angiogenesis-stimulation artificial ligament for anterior cruciate ligament reconstruction, Acta Biomater. 54 (2017) 399–410.

[52] J. Wang, J. Xu, W. Fu, W. Cheng, K. Chan, P.S.-h. Yung, L. Qin, Biodegradable magnesium screws accelerate fibrous tissue mineralization at the tendon-bone insertion in anterior cruciate ligament reconstruction model of rabbit, Sci. Rep. 7 (1) (2017) 1–12.

[53] J. Wang, J. Xu, X. Wang, L. Sheng, L. Zheng, B. Song, G. Wu, R. Zhang, H. Yao, N. Zheng, Magnesium-pretreated periosteum for promoting bone-tendon healing after anterior cruciate ligament reconstruction, Biomaterials 268 (2021) 120576.

[54] J.-C. Zong, R. Ma, H. Wang, G.-T. Cong, A. Lebaschi, X.-H. Deng, S.A. Rodeo, The effect of graft pretensioning on bone tunnel diameter and bone formation after anterior cruciate ligament reconstruction in a rat model: evaluation with micro–computed tomography, Am. J. Sports Med. 45 (6) (2017) 1349–1358.

[55] Q. Cai, F. Chen, F. Xu, K. Wang, K. Zhang, G. Li, J. Chen, H. Deng, Q. He, Epigenetic silencing of microRNA-125b-5p promotes liver fibrosis in nonalcoholic fatty liver disease via integrin α8-mediated activation of RhoA signaling pathway, Metabolism 104 (2020), 154140.

[56] H. Cui, Y. He, S. Chen, D. Zhang, Y. Yu, C. Fan, Macrophage-derived miRNA-containing exosomes induce peritendinous fibrosis after tendon injury through the miR-21-5p/Smad7 pathway, Mol. Ther. Nucleic Acids 14 (2019) 114–130.

[57] Y. Liu, Z.-J. Dong, J.-W. Song, L.-R. Liang, L.-L. Sun, X.-Y. Liu, R. Miao, Y.-L. Xu, X.-T. Li, M.-W. Zhang, MicroRNA-122–5p promotes renal fibrosis and injury in spontaneously hypertensive rats by targeting FOXO3, Exp. Cell Res. 411 (2) (2022), 113017.

[58] T. Sing, M. Jinnin, K. Yamane, N. Honda, K. Makino, I. Kajihara, T. Makino, K. Sakai, S. Masuguchi, S. Fukushima, microRNA-92a expression in the sera and dermal fibroblasts increases in patients with scleroderma, Rheumatology (Oxford) 51 (9) (2012) 1550–1556.

[59] S.K. Venugopal, J. Jiang, T.-H. Kim, Y. Li, S.-S. Wang, N.J. Torok, J. Wu, M.A. Zern, Liver fibrosis causes downregulation of miRNA-150 and miRNA-194 in hepatic stellate cells, and their overexpression causes decreased stellate cell activation, Am. J. Physiol. Gastrointest. Liver Physiol. 298 (1) (2010) G101–G106.

[60] B. Wang, M. Xu, M. Li, F. Wu, S. Hu, X. Chen, L. Zhao, Z. Huang, F. Lan, D. Liu, Mir-25 promotes cardiomyocyte proliferation by targeting fbxw7, Mol. Ther. Nucleic Acids 19 (2020) 1299–1308.

[61] G. Anders, S.D. Mackowiak, M. Jens, J. Maaskola, A. Kuntzagk, N. Rajewsky, M. Landthaler, C. Dieterich, doRiNA: a database of RNA interactions in post-transcriptional regulation, Nucleic Acids Res. 40 (D1) (2012) D180–D186.

[62] D. Betel, M. Wilson, A. Gabow, D.S. Marks, C. Sander, The microRNA. org resource: targets and expression, Nucleic Acids Res. 36 (suppl_1) (2008) D149–D153.

[63] R.C. Friedman, K.K.-H. Farh, C.B. Burge, D.P. Bartel, Most mammalian mRNAs are conserved targets of microRNAs, Genome Res. 19 (1) (2009) 92–105.

[64] A. Grimson, K.K.-H. Farh, W.K. Johnston, P. Garrett-Engele, L.P. Lim, D.P. Bartel, MicroRNA targeting specificity in mammals: determinants beyond seed pairing, Mol. Cell 27 (1) (2007) 91–105.

[65] M. Kertesz, N. Iovino, U. Unnerstall, U. Gaul, E. Segal, The role of site accessibility in microRNA target recognition, Nat. Genet. 39 (10) (2007) 1278–1284.

[66] B.P. Lewis, C.B. Burge, D.P. Bartel, Conserved seed pairing, often flanked by adenosines, indicates that thousands of human genes are microRNA targets, Cell 120 (1) (2005) 15–20.

[67] D. Szklarczyk, J.H. Morris, H. Cook, M. Kuhn, S. Wyder, M. Simonovic, A. Santos, N.T. Doncheva, A. Roth, P. Bork, The STRING database in 2017: quality-controlled protein–protein association networks, made broadly accessible, Nucleic Acids Res. 45 (D1) (2017) D362–D368.

[68] P. Shannon, A. Markiel, O. Ozier, N.S. Baliga, J.T. Wang, D. Ramage, N. Amin, B. Schwikowski, T. Ideker, Cytoscape: a software environment for integrated models of biomolecular interaction networks, Genome Res. 13 (11) (2003) 2498–2504.

[69] P.L. Hays, S. Kawamura, X.-H. Deng, E. Dagher, K. Mithoefer, L. Ying, S.A. Rodeo, The role of macrophages in early healing of a tendon graft in a bone tunnel, J. Bone Joint Surg. Am. 90 (3) (2008) 565–579.

[70] F.H. Fu, C.H. Bennett, C. Lattermann, C.B. Ma, Current trends in anterior cruciate ligament reconstruction, Am. J. Sports Med. 27 (6) (1999) 821–830.

[71] C.D. Papageorgiou, C.B. Ma, S.D. Abramowitch, T.D. Clineff, S.L. Woo, A multidisciplinary study of the healing of an intraarticular anterior cruciate ligament graft in a goat model, Am. J. Sports Med. 29 (5) (2001) 620–626.

[72] F. Tomita, K. Yasuda, S. Mikami, T. Sakai, S. Yamazaki, H. Tohyama, Comparisons of intraosseous graft healing between the doubled flexor tendon graft and the bone–patellar tendon–bone graft in anterior cruciate ligament reconstruction, Arthroscopy 17 (5) (2001) 461–476.

[73] J.-R. Lee, B.-W. Park, J. Kim, Y.W. Choo, H.Y. Kim, J.-K. Yoon, H. Kim, J.-W. Hwang, M. Kang, S.P. Kwon, Nanovesicles derived from iron oxide nanoparticles–incorporated mesenchymal stem cells for cardiac repair, Sci. Adv. 6 (18) (2020), eaaz0952.

[74] Z. Wen, S. Zheng, C. Zhou, W. Yuan, J. Wang, T. Wang, Bone marrow mesenchymal stem cells for post-myocardial infarction cardiac repair: micrornas as novel regulators, J. Cell Mol. Med. 16 (4) (2012) 657–671.

[75] P. Lui, Y. Lee, T. Mok, Y. Cheuk, K. Chan, Alendronate reduced peri-tunnel bone loss and enhanced tendon graft to bone tunnel healing in anterior cruciate ligament reconstruction, Eur. Cell. Mater. 25 (2013) 78–96.

[76] P.P.Y. Lui, Y.W. Lee, T.Y. Mok, Y.C. Cheuk, Peri-tunnel bone loss: does it affect early tendon graft to bone tunnel healing after ACL reconstruction? Knee Surg. Sports Traumatol. Arthrosc. 23 (3) (2015) 740–751.

[77] K. Marycz, P. Sobierajska, M. Roecken, K. Kornicka-Garbowska, M. Kępska, R. Idczak, J.-M. Nedelec, R.J. Wiglusz, Iron oxides nanoparticles (IOs) exposed to magnetic field promote expression of osteogenic markers in osteoblasts through integrin alpha-3 (INTa-3) activation, inhibits osteoclasts activity and exerts anti-inflammatory action, J. Nanobiotechnol. 18 (1) (2020) 1–24.

[78] K. Marycz, P. Sobierajska, R. Wiglusz, R. Idczak, J.-M. Nedelec, A. Fal, K. Kornicka-Garbowska, Fe 3 O 4 magnetic nanoparticles under static magnetic field improve osteogenesis via RUNX-2 and inhibit osteoclastogenesis by the induction of apoptosis, Int. J. Nanomed. 15 (2020) 10127–10148.

[79] M. Benjamin, J. Ralphs, Fibrocartilage in tendons and ligaments—an adaptation to compressive load, J. Anat. 193 (4) (1998) 481–494.

[80] A. Chainani, D. Little, Current status of tissue-engineered scaffolds for rotator cuff repair, Tech. Orthop. 31 (2) (2016) 91–97.

[81] P. Randelli, A. Menon, V. Ragone, P. Creo, S. Bergante, F. Randelli, L. De Girolamo, U. Alfieri Montrasio, G. Banfi, P. Cabitza, Lipogems product treatment increases the proliferation rate of human tendon stem cells without affecting their stemness and differentiation capability, Stem Cell. Int. 2016 (2016), 4373410.

[82] T. Yoshikawa, H. Tohyama, T. Katsura, E. Kondo, Y. Kotani, H. Matsumoto, Y. Toyama, K. Yasuda, Effects of local administration of vascular endothelial growth factor on mechanical characteristics of the semitendinosus tendon graft after anterior cruciate ligament reconstruction in sheep, Am. J. Sports Med. 34 (12) (2006) 1918–1925.

[83] Y. Huang, B. He, L. Wang, B. Yuan, H. Shu, F. Zhang, L. Sun, Bone marrow mesenchymal stem cell-derived exosomes promote rotator cuff tendon-bone healing by promoting angiogenesis and regulating M1 macrophages in rats, Stem Cell Res. Ther. 11 (1) (2020) 1–16.

[84] S.G. Dakin, MicroRNA replacement: a new era of Mol Ther for tendon disorders? Mol. Ther. 25 (10) (2017) 2243–2244.

[85] E. Ardite, E. Perdiguero, B. Vidal, S. Gutarra, A.L. Serrano, P. Muñoz-Cánoves, PAI-1–regulated miR-21 defines a novel age-associated fibrogenic pathway in muscular dystrophy, J. Cell Biol. 196 (1) (2012) 163–175.

[86] A.D. McClelland, M. Herman-Edelstein, R. Komers, J.C. Jha, C.E. Winbanks, S. Hagiwara, P. Gregorevic, P. Kantharidis, M.E. Cooper, miR-21 promotes renal fibrosis in diabetic nephropathy by targeting PTEN and SMAD7, Clin. Sci. (Lond.) 129 (12) (2015) 1237–1249.

[87] L. Ding, M. Wang, S. Qin, L. Xu, The roles of MicroRNAs in tendon healing and regeneration, Front. Cell Dev. Biol. 9 (2021).

[88] W. Zheng, J. Song, Y. Zhang, S. Chen, H. Ruan, C. Fan, Metformin prevents peritendinous fibrosis by inhibiting transforming growth factor-β signaling, Oncotarget 8 (60) (2017), 101784.

[89] H. Zhou, S. Jiang, P. Li, H. Shen, H. Yang, S. Xu, C. Ye, M. Chen, H. Lu, Improved tendon healing by a combination of Tanshinone IIA and miR-29b inhibitor treatment through preventing tendon adhesion and enhancing tendon strength, Int. J. Med. Sci. 17 (8) (2020) 1083.

[90] P.Ö. Eser, P.A. Jänne, TGFβ pathway inhibition in the treatment of non-small cell lung cancer, Pharmacol. Ther. 184 (2018) 112–130.

[91] H.-H. Hu, D.-Q. Chen, Y.-N. Wang, Y.-L. Feng, G. Cao, N.D. Vaziri, Y.-Y. Zhao, New insights into TGF-β/Smad signaling in tissue fibrosis, Chem. Biol. Interact. 292 (2018) 76–83.

[92] X. Yan, Z. Liu, Y. Chen, Regulation of TGF-β signaling by Smad7, Acta Biochim. Biophys. Sin. 41 (4) (2009) 263–272.